Experimental Mechanics (2023) 63:529–563
https://doi.org/10.1007/s11340-022-00932-9

RESEARCH PAPER

Uncertainty Analysis of Dynamic Rupture Measurements Obtained Through Ultrahigh-Speed Digital Image Correlation

A. Lattanzi[1] · V. Rubino[2] · M. Rossi[1] · A. Donzelli[2] · A.J. Rosakis[2] · N. Lapusta[3,4]

Received: 4 October 2022 / Accepted: 28 November 2022 / Published online: 4 January 2023

Abstract

Background The full-field behavior of dynamic shear cracks, with their highly transient features, has recently been quantified by employing Digital Image Correlation (DIC) coupled with ultrahigh-speed photography (at 1-2 million frames/sec). The use of ultrahigh-speed DIC has enabled the observation of complex structures associated with the evolution of the dynamic shear fractures under controlled laboratory conditions, providing a detailed description of their distinctive full-field kinematic features. This has allowed to identify, for instance, the spatiotemporal characteristics of sub-Rayleigh and intersonic shear ruptures, and to measure the evolution of dynamic friction during rupture propagation of frictional shear ruptures.

Objective Capturing such highly transient phenomena represents a challenging metrological process influenced by both ultra-fast imaging procedures and DIC analysis parameters. However, the effect of these parameters on the quantification of the rupture features has not been assessed yet. Here, a simulated experiment framework is presented and employed to evaluate the uncertainties associated with ultrahigh-speed DIC measurements.

Methods Finite element simulations replicate laboratory experiments of dynamic ruptures spontaneously propagating along frictional interfaces. Experimental images of the specimen acquired with an ultrahigh-speed camera are numerically deformed by the displacement fields obtained from the numerical simulations and are analyzed using the same DIC analysis procedure as in the laboratory experiments.

Results The displacement, particle velocity, and strain fields obtained from the DIC analysis are compared with the ground-truth fields of the numerical simulations, correlating the measurement resolution with the physical length scale of the propagating Mode II rupture. In addition, the full-field data are employed to estimate the capability of the ultrahigh-speed DIC setup to infer the dynamic friction evolution.

Conclusions This methodology allows us to quantify the accuracy of the ultrahigh-speed DIC measurements in resolving the complex spatiotemporal structures of dynamic shear ruptures, focusing on the impact of the key correlation parameters.

Keywords Dynamic shear rupture · Digital Image Correlation · Error assessment · Virtual experiments

✉ A. Lattanzi
a.lattanzi@staff.univpm.it

V. Rubino
vito.rubino@caltech.edu

M. Rossi
m.rossi@staff.univpm.it

A. Donzelli
alexdonz@caltech.edu

A.J. Rosakis
arosakis@caltech.edu

N. Lapusta
lapusta@caltech.edu

[1] Department of Industrial Engineering and Mathematical Sciences, Università Politecnica delle Marche, Ancona 60131, Italy

[2] Graduate Aerospace Laboratories, California Institute of Technology, Pasadena 91125, CA, USA

[3] Department of Mechanical and Civil Engineering, California Institute of Technology, Pasadena 91125, CA, USA

[4] Seismological Laboratory, California Institute of Technology, Pasadena 91125, CA, USA

Introduction

The study of dynamic shear cracks along frictional interfaces is relevant for a wide spectrum of engineering and applied sciences applications, ranging from fiber delamination in fiber reinforced-composites to earthquake mechanics [1–4]. The Digital Image Correlation (DIC) method, one of the most established full-field approaches [5, 6] has been employed in an increasing number of applications [7, 8], including challenging engineering problems such as strain localization [9], microstructure measurements [10], high temperature [11], volume deformation [12] etc. Recently, the advance in the ultrahigh-speed cameras technology is fostering the use of DIC and full-field measurement in the high-strain-rate dynamic range [13–16]. The DIC technique compares digital images containing a characteristic gray-level texture, in deformed and undeformed configurations, using patterns matching algorithms to determine the displacement fields, and subsequently obtain derived quantities such as strains or particle velocities [5]. The DIC method has been used to study the static field of dynamic cracks (e.g. [17]) and has been applied to a variety of dynamic settings [18–23]. However, the characterization of the full-field behavior of dynamic cracks and other highly transient processes has been hindered by limitations in high-speed camera technology capable of providing adequate spatial and temporal resolution at low noise level.

Recently, the use of DIC coupled with the new generation of ultrahigh-speed cameras has made possible the quantification of full-field displacements, velocities and strains of dynamic shear cracks [16, 24, 25]. This development has enhanced the understanding of rupture dynamics by enabling new observations, including quantifying the near-field behavior of sub-Rayleigh and supershear ruptures [25, 26], tracking the local evolution of friction during dynamic rupture propagation [24, 27, 28], and discovering the formation of pressure shock fronts associated with the spontaneous propagation of shear cracks [29]. Capturing ruptures propagating at speeds of the order of 1 km/s presents several challenges due to the highly transient and heterogeneous nature of the fields involved. An important requirement for the DIC analysis to produce derived quantities such as strains and velocities is low-noise-level images. The current ultrahigh-speed imaging technology is capable of reaching adequately high-frame rates with a camera noise suitable for the DIC analysis [30, 31], but at the cost of low image resolution. At the same time, spatial resolution is also an important requirement for the observation of the fine features associated dynamic rupture propagation. One way to compromise between spatial resolution and noise mitigation is to adopt multiple fields of view, designed to either capture the far-field behavior or accurately quantify the near-field characteristics [25].

An initial validation of these dynamic measurements was performed by comparing the particle velocities produced by DIC to simultaneous measurements obtained with the well-established technique of laser velocimetry [32], at the same locations [24, 25]. While these comparisons provide confidence in the accuracy of the DIC measurements, they are nonetheless point-wise comparisons and do not fully characterize the measurement errors. An initial estimate of the measurement uncertainties associated with the DIC analysis, as well as with experimental sources such as camera noise, speckle pattern, and environmental factors (e.g lighting variations during the image acquisition) was assessed by comparing nominally identical images [25]. However, these approaches do not quantify the capability of DIC measurements to capture the highly heterogeneous fields associated with dynamic ruptures.

In this study, we focus on investigating the accuracy of DIC measurements by comparing them to the ground-truth provided by virtual experiments of dynamic shear ruptures. In particular, we concentrate on the study ruptures propagating at supershear speeds, faster than the shear wave speed. These ruptures are particularly challenging to capture with DIC measurements as they are characterized by sharp features associated with the formation of shear Mach fronts [16, 26]. The virtual experiments are generated by deforming experimental images using the displacement fields obtained by finite element simulations of the laboratory experiments of [16, 25]. This methodology has proven in the past to be a reliable approach to investigate the accuracy of full-field measurements in complex experiments and setups [33–40]. For instance, Rossi et al. [35] developed a numerical simulator to estimate the errors associated with the full-field measurements produced by DIC and the Grid Method [41], and investigated the error propagation chain in the identification of material properties using an inverse method, i.e. the virtual fields method [42]. A similar approach was also presented in [36], where simulated tensile tests were employed to determine the effects of DIC uncertainties (i.e. out of plane motions, camera noise, light conditions) on the identification of the elastic properties of an aluminum alloy with the VFM. These studies assumed a 2D-DIC system. A first example of 3D-DIC simulator aimed at quantifying the uncertainties corresponding to the more complex stereo measurement was presented in [43, 44]. In addition, virtual DIC experiments have been involved in the design and optimization of advanced material tests, including the characterization of composite materials [45] and foams [46], and for the development of novel high-strain rate tests [47, 48].

The virtual experiment framework presented in this paper, obtained by numerically simulating the laboratory experiments of [25], provides a digital twin of the whole DIC measurement chain of the test. This approach opens up the exploration of the influence of DIC settings on the observation of all kinematic quantities characterizing the fracture evolutionary pattern and their optimization, which can have important implications for the interpretation of the results.

The paper is organized as follows: "Laboratory Experiments Capturing Dynamic Shear Ruptures Using Ultrahigh-speed DIC" section describes the experimental setup; "Virtual-experiment Framework to ValidateDIC Measurements" section details the Virtual Experiment framework, illustrating the steps for the generation of synthetic images, starting from a numerical simulation of the test. The DIC error is characterized in "Characterization of the Full-field Measurement Uncertainties" section, where we compare the full-field displacement, velocity and strain components obtained with the DIC analysis with the reference numerical counterparts. Finally, "Reconstructing the Friction Behaviour fromDIC Measurements" section is dedicated to a preliminary analysis of the uncertainties associated with friction measurements from ultrahigh-speed DIC maps.

Laboratory Experiments Capturing Dynamic Shear Ruptures Using Ultrahigh-speed DIC

Dynamic shear cracks are produced in the laboratory as frictional ruptures along the interface formed by two plates of a polymeric material (typically Homalite-100 or PMMA), inclined by an angle α (Fig. 1(a)) [25]. A vertical load P, applied on the specimen by a servo-hydraulic loading machine, results in a normal and shear pre-stress level on the interface given by $\sigma_0 = P\cos^2\alpha$ and $\tau_0 = P\cos\alpha\sin\alpha$, respectively. Ruptures are nucleated by a small burst of a NiCr wire placed across the interface. This experimental setup reproduces the main features of earthquake ruptures propagating along pre-existing faults in the Earth's crust and has been employed to investigate key earthquake rupture features, initially using diagnostics based on photoelasticity and laser velocimetry (e.g. [49–52]), and later using digital image correlation [16, 17, 24, 26–29]. The previous set of diagnostics provided temporally accurate but spatially sparse velocity measurements through laser interferometry and fringe plots of the maximum shear stress [51] but could not provide individual stress components or other full-field measurements.

The current version of the experimental setup featuring digital image correlation coupled with ultrahigh-speed photography allows the measurement of full-field displacements, particle velocities, and strains [25]. A Shimadzu® HPV-X camera records a sequence of 128 images of a portion of the specimen at 1-2 million frames/s with a resolution of 400×250 pixel^2. A portion of the specimen to be imaged is covered by a white coating first and then by a black speckle pattern, in order to provide a characteristic texture for image matching. This pattern is produced using a dot-on-dot technique, where the size of the features is set depending on the field of view, so as to be in the range of 3-6 pixels (Fig. 3). The use of a dotted pattern, over traditional spray painted patterns, allows to accurately control the speckle size with the purpose of minimizing spatial aliasing and maximize spatial resolution [25]. This is particularly important when using ultrahigh-speed cameras with a low fill factor, where small features may go undetected. The size of the field of view is chosen depending on whether the aim of test is to capture the far- or the near-field structure. Two typical selections of fields of view are shown in Fig. 1(a), and snapshots of the measured displacement fields of the propagating rupture corresponding to the large field of view are displayed in Fig. 1(b).

The image sequence is then analyzed with a digital image correlation algorithm, using the commercial software VIC-2D (Correlated Solution® Inc.), which employs a subset-based DIC formulation.

In order to capture the inherent displacement discontinuities across the interface characterizing shear ruptures, two independent analysis domains are defined, above and below the specimen interface. If a single domain were used for the whole field of view, the subsets overlapping the interface would result in averaging displacements across regions governed by opposite sign of motion. Instead, the "fill-boundary" algorithm of VIC-2D is employed to extrapolate the displacements from the subset centers to the boundary of the domain, i.e. the interface, using affine transformation functions.

The full-field particle velocity and strain maps are obtained from the raw displacement fields using a finite difference scheme, as detailed in Appendix 2; furthermore, in actual experiments, filters are applied to the full-field data in order to reduce the measurement noise [24, 25, 27]. The present study, however, is focused on the bias introduced by the correlation algorithm and the speckle pattern, therefore the synthetic images are generated without introducing noise and no smoothing is used in the postprocessing. A detailed assessment of the effect of noise and smoothing will be tackled in future works.

Virtual-experiment Framework to Validate DIC Measurements

To investigate the accuracy of dynamic shear rupture measurements obtained with ultrahigh-speed DIC, we employ a virtual experiment-framework where the ground-truth is given by Finite Element (FE) simulations of the experiments. The FEM simulations provide a similar displacement distribution, capturing the steep gradients associated with the propagation of dynamic shear cracks. An experimental image of the specimen, containing the same speckle pattern used in the experiments

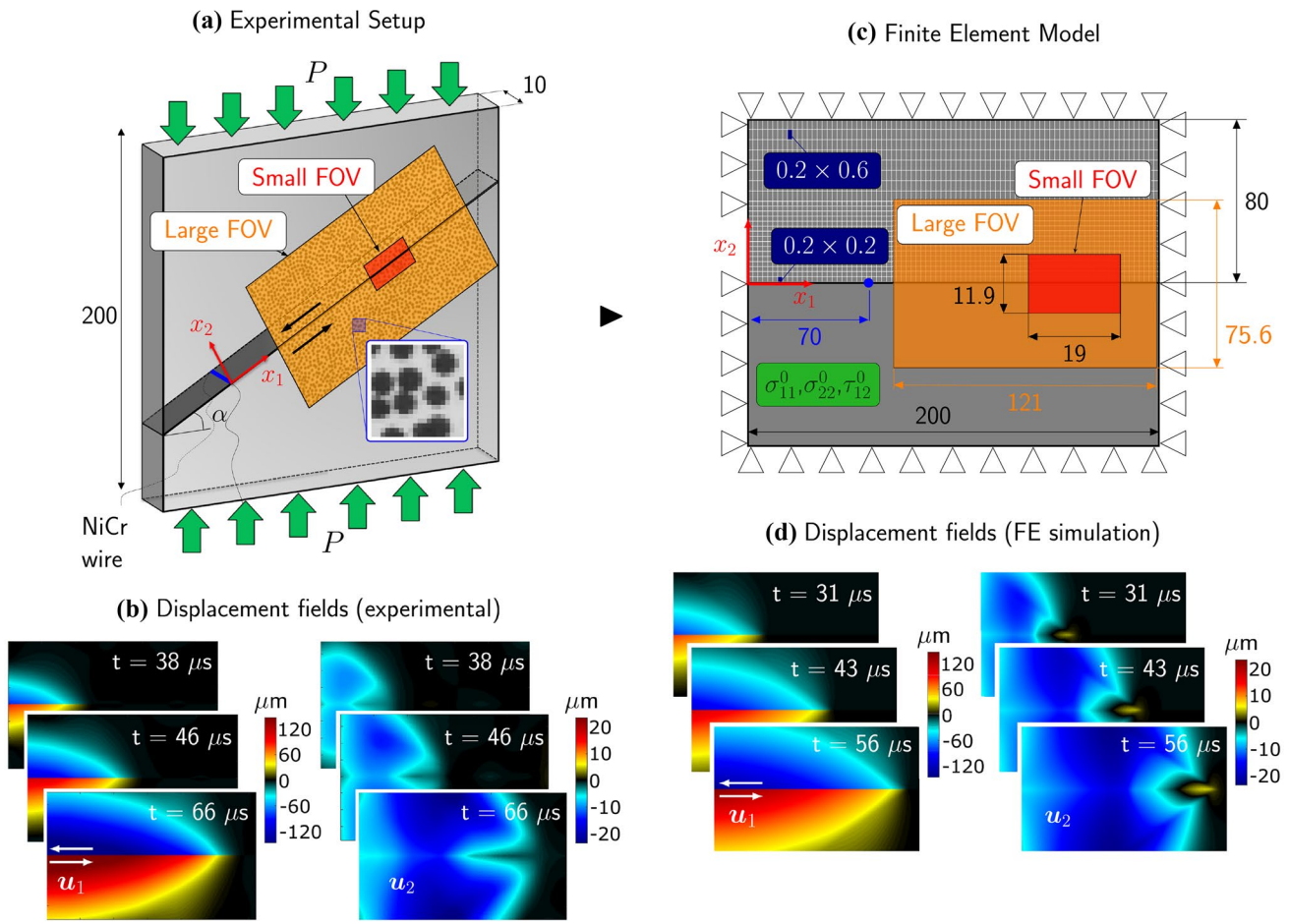

Fig. 1 Schematics of the experimental setup employed to study dynamic shear ruptures in the laboratory in [25] and its numerical modeling in this study. (**a**) Dynamic shear cracks are generated along the frictional interface of two Homalite-100 plates. The pre-load P enforces static compression and shear stresses on the contact surface inclined at the angle α, while the rupture is nucleated through the small burst of a NiCr wire placed across the interface. (**c**) The finite element model used to produce synthetic images to be analyzed with DIC. The figure shows the size of the two fields of view (FOV) employed in this study, referred to as large (orange) and small FOV (red). The reference frame is chosen with axes parallel (x_1) and perpendicular (x_2) to the interface. The portion above the interface shows the discretization of the finite element mesh, featuring smaller elements close to the interface in order to resolve higher gradients near the rupture tip. The nucleation site along the interface is shown as a blue dot. All dimensions are given in mm. Examples of displacement fields at $P = 23$ MPa and $\alpha = 29°$ measured by means of ultrahigh-speed DIC during a laboratory experiment and computed from the numerical simulation are reported in (**b**) and (**d**) respectively

[25], is acquired with the ultrahigh-speed camera and is deformed according to the displacement fields obtained from the FEM simulations (Fig. 2). The deformed images are then analyzed with the same DIC algorithms used for the laboratory experiments described in "Laboratory Experiments Capturing Dynamic Shear Ruptures Using Ultrahigh-speed DIC" section. Finally, the displacement, velocity, and strain fields obtained with the DIC analysis are compared with the corresponding ground-truth fields provided by the FEM simulations.

Finite Element Model of the Laboratory Experiments

The laboratory earthquake experiment described in "Laboratory Experiments Capturing Dynamic Shear Ruptures Using Ultrahigh-speed DIC" section is replicated by a finite element model in *ABAQUS/Explicit*® using 4-node reduced integration elements (CPS4R). As depicted in Fig. 1(c), two plates are placed in contact and loaded in compression and shear by $\sigma^0_{22} = P\cos^2\alpha$ and $\tau^0_{12} = P\cos\alpha\sin\alpha$, respectively. The geometry and boundary conditions of this model are inspired by the model of Lu et al. [53]. The simulations of Lu et al. were performed using the boundary-integral method [54, 55], which is efficient at reproducing the rupture physics, but does not provide the displacement fields in the bulk.

In the present simulations, we take $P = 23$ MPa and $\alpha = 29°$, as in the experiments of [25]. Plane stress conditions are assumed, due to the small thickness of the specimen (10 mm) with respect to the other dimensions. To improve the computational efficiency

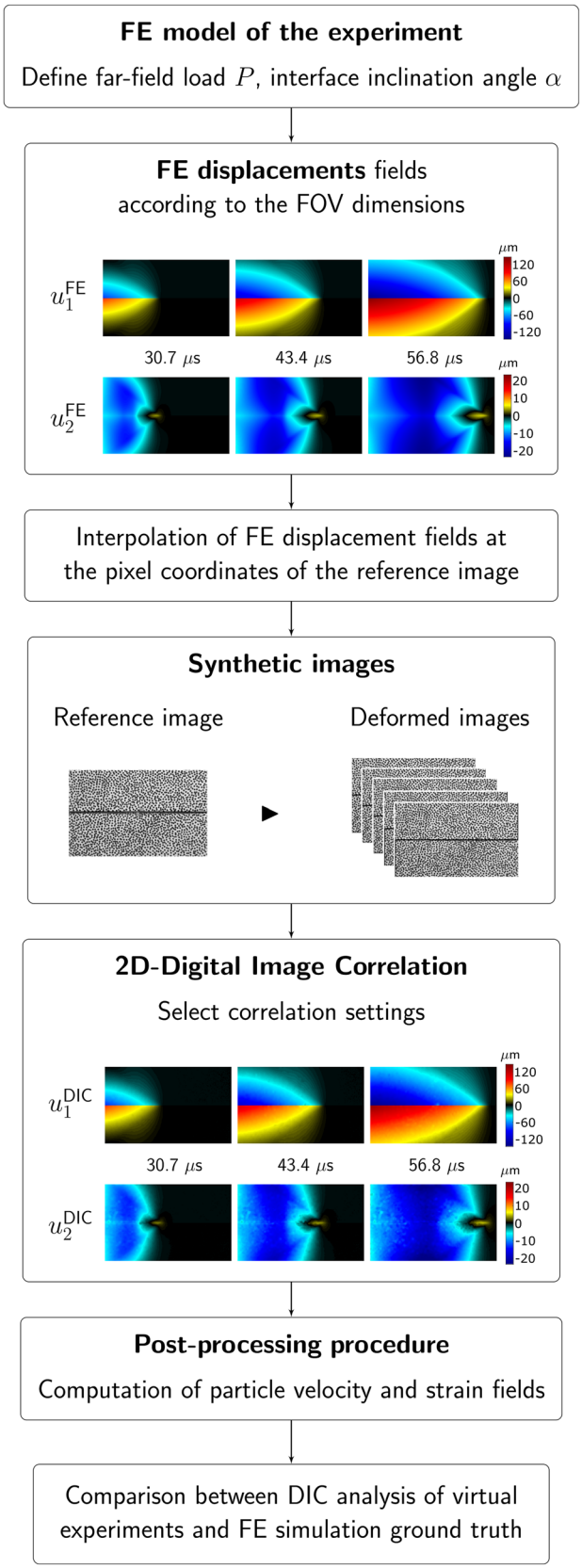

◀ **Fig. 2** Flowchart of the virtual experiment: the displacement fields produced by a finite element (FE) simulation of the test are used to deform a reference speckle patterned image; the procedure generates a temporal sequence of numerically deformed images; the deformed images are subsequently analysed by using the DIC technique. Finally, the measured field quantities are compared with the FEM ground-truth to assess the measurement uncertainties

of the model, each plate is horizontally partitioned into equal halves, with the portions close to the interface discretized by 0.2×0.2 mm elements, and those further away by 0.2×0.6 mm elements. Overall, each plate is composed of 285285 elements and 286572 nodes.

In our model, we use effective linear-elastic properties, with the dynamic, high-strain-rate Young's modulus of Homalite-100 [56]. Homalite-100 is a strain-rate dependent polymer [56] and the dependence on strain rate has been shown to influence its full-field behavior [29]. An comparison of the full-field maps of displacements, velocities and strains produced by the finite element simulations with the experimental counterparts indicate that the FEM simulations contain most of the complexities and characteristic features of the experimental ruptures. However, since these simulations do not fully incorporate the viscoelastic properties of Homalite-100, they should not be considered direct simulations of the experiment, in their present form, but rather a close representation. The material properties of Homalite-100 used in the simulations are listed in Table 1.

In the numerical model, the pre-stress conditions given by the far-field loading are applied on each node, at the beginning of the simulation, by assigning the corresponding stress components as predefined fields. In addition to the shear and interface-normal pre-stresses mentioned above, the interface-parallel component of pre-stress is $\sigma_{11}^0 = P\cos^2\alpha$. All displacements of nodes placed on the external borders of the specimen are blocked.

The propagation of dynamic ruptures is controlled by the frictional shear resistance and its evolution with slip and slip rate. In our FEM model, we employ a commonly used friction law, the slip-weakening formulation of friction [55, 57–59], in which the friction coefficient f linearly degrades

Table 1 Material properties of Homalite-100 adopted in the numerical model

Dynamic Young's modulus E (MPa)	5300
Poisson ratio ν	0.35
Density ρ (kg/m^3)	1200
Pressure wave speed c_p (m/s)	2498
Shear wave speed c_s (m/s)	1200

with slip δ from its static value f_s, to a residual, dynamic level f_d, over a lengthscale D_c (Appendix 1). In the linear slip-weakening formulation, f_s, f_d, and D_c are considered as material parameters. In reality, these parameters are not constants, and friction evolution is controlled by the slip rate and its history, as well other effects [2, 16, 60]. However, linear slip-weakening can be used as an effective law, and f_s, f_d and D_c can be considered effective parameters [16]. Here we employ $f_s = 0.65$, $f_d = 0.26$ and $D_c = 25$ μm obtained experimentally [24] under the same loading conditions as used in the simulations. The linear slip-weakening law is implemented in the FEM solver though a VFRIC user subroutine adopting a split node contact procedure [58].

The contact between the two plates is modeled by employing the internal Abaqus® Penalty algorithm, with the pressure-overclosure behaviour assumed as "hard". This method is usually used to handle a wide number of contact problems due to its very general formulation, but introduces an additional stiffness behaviour to the model that, in turn, can influence the stable time increment. As consequence, a relatively small time increment of 0.00128 μs is used to ensure the numerical stability of the solution.

At the initial stage, the two plates are in equilibrium under the static loading, due to the shear pre-stress being lower than the peak shear frictional strength. The sudden pressure release – provided by the expansion of the NiCr wire – initiating the experimental ruptures is replicated in the FEM model by locally reducing the frictional strength in a small portion of the interface, as detailed in Appendix 1.

Numerical Procedure to Deform the Experimental Images

An experimental image of the specimen, containing the speckle pattern, is deformed using the approach introduced by Rossi et al. [35]. The approach is graphically summarized in Fig. 2. The reference image containing the speckle pattern can be obtained either experimentally or numerically. In this case, the image is taken in the laboratory by a Shimadzu® HPV-X ultrahigh-speed camera (400×250 pixel^2) in the same conditions (speckle pattern, illumination, etc.) and using the same camera parameters (frame rate and exposure time) as in an actual dynamic test [25]. Using an experimental image allows us to include realistic features of the experiment in the DIC analysis. To isolate the effects of the analysis parameters and post-processing procedure, we synthetically deform one experimental image with the evolving displacements fields. In future studies, we plan to deform an actual sequence of experimental images to also include the effects of camera and ambient noise.

Due to the reduced image resolution of the ultrahigh-speed camera, the process of synthetically deforming the image can induce numerical noise into the images, which can be wrongly interpreted as due to lower accuracy of the DIC measurement in capturing sub-pixel displacements. In order to mitigate this artificial effect, one effective strategy is to deform images with an augmented resolution and later perform a pixel subsampling to restore the initial image size [61–63]. This method has been validated by Rossi et al. in [35] by evaluating the measurement error associated with synthetically shifting images by a sub-pixel amount and comparing the results with other deformation algorithms, such as the Fast Fourier Transform and Binning techniques [61]. The initial reference image resolution is increased by a scale factor $s_f = 9$, so that each pixel of the low-resolution image is decomposed into a 9×9 sub-pixel matrix in the high-resolution image.

The deformed images are generated according to a two-step interpolation procedure. First, the elements within the selected FOV are extracted from the numerical simulation, and the corresponding nodal displacements are mapped onto 3600×2250 arrays by means of a bi-linear interpolation. Then, the high-resolution reference image is deformed by enforcing the interpolated displacement fields on each pixel integer position. The process leads to a 16-bit gray level map whose values are placed at non-integer positions. Thus, a second interpolation is performed to compute the gray values at the pixel integer locations, obtaining the high-resolution deformed image.

Finally, before performing the DIC analysis, the deformed, high-resolution images are subsampled in order to produce images of the same size as they would be obtained from the ultrahigh-speed camera in a laboratory experiment. In particular, the gray level of each pixel of the 400×250 pixel^2 image is calculated by convolving the gray levels of the corresponding sub-pixel matrix. Note that the pixel subsampling must be performed on both reference and deformed images in order to have a valid correlation in the DIC analysis.

The FEM model simulates the shear rupture evolution up to 62 μs after rupture initiation. Considering a temporal sampling of the HPV-X high-speed camera of 2 million fps, the virtual experiment output results in a sequence 125 images of the speckle pattern deformed by the propagating dynamic rupture.

Characterization of the Full-field Measurement Uncertainties

Two standard approaches to characterize full-field measurement uncertainties are based on [37]: (i) analyzing nominally identical (undeformed) images of the speckled pattern; (ii) correlating pre-specified in-plane and out-of-plane rigid-body translations of the specimen. These approaches can determine the effect of correlation algorithm, noise and other environmental factors on the measurement error. While these methods provide a first-order estimate of the measurement uncertainties, they cannot quantify the capability of the

correlation algorithm to capture the full-field deformation structure. In order to test the theoretical limit of the correlation algorithm to reconstruct the full-field features associated with dynamic shear fractures, we use simulated experiments deforming the speckle pattern according to theoretical displacement fields. In this study, we deform noiseless images. The absence of electronic noise and other experimental uncertainties in the images allows us to isolate the uncertainties produced by the analysis parameters. In a future study, we will analyze noisy images to study the combined effect of deformations and noise in the correlation process.

The numerically-deformed images generated through the virtual experiment procedure can guide us to an accurate choice of the analysis parameters for a reliable reproduction of the details characterizing the structure of dynamic ruptures. In particular, the subset size is a key analysis parameter determining the capability to resolve the field quantities, the spatial resolution, and the noise level of the DIC measurement. In the analysis of dynamic ruptures studied here, the choice of the subset size is particularly challenging because the analysis is performed on images with a relatively small resolution, and the sharp features produced by the rupture have the size of few pixels. While relatively smaller subset sizes are preferable as they can more accurately capture the signal amplitude, they also result in higher noise levels, which are particularly detrimental to obtain derived quantities, such as particle velocities, strains, or strain rates. This study aims to investigate the effect of the subset size and shape function formulation on the measured field structures.

Let us compare the full-field displacement, velocity, and strain maps obtained with DIC are with the corresponding "actual" maps produced by the FEM simulations. The DIC maps are obtained by using the following subset sizes: 11×11 pixel^2, 21×21 pixel^2, 31×31 pixel^2, 41×41 pixel^2, 51×51 pixel^2 (see Fig. 3). The subset-size effect

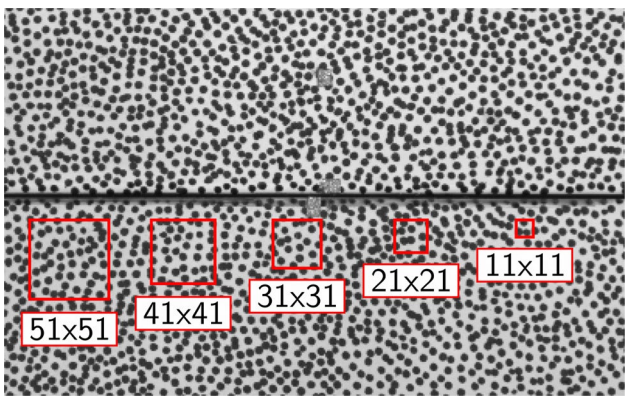

Fig. 3 Adopted speckle pattern for the synthetic image generation. The pattern is the same for both the considered FOVs, thus, the pattern size is the same in pixels but different in physical dimensions. The different subset sizes (in pixel) are reported for comparison

is explored by employing a shape function with an affine transformation order. The influence of higher order quadratic transformation function is examined in "Effect of the Order of Subset Transformation Functions". The DIC parameters and settings adopted in this study are detailed in Table 2, as recommended by the good-practices guide of the International DIC Society (iDICs) [64].

We investigate the effects of two different fields of view (FOV), referred to as "large" and "small" FOVs, whose dimensions, shown in Fig. 1(c), mimic those used experimentally [25]. As mentioned above, the choice of these two different fields of view is dictated on the one hand by the need to visualize the rupture patterns at relatively large distances from the interface, and on the other hand by the need to resolve fine rupture features in the near-crack-tip region that would not be possible to capture with large fields of view.

The analysis of the uncertainties associated with the DIC measurement follows a two-step approach in this study (Fig. 4). First, the DIC-measured full-field maps are compared with the corresponding FEM maps. The FEM maps are obtained through the interpolation of the nodal solution onto a 400×250 pixel^2 regular grid, according to the field of view dimensions. The uncertainties associated with the DIC measurements are highlighted by examining the point-by-point difference between the FEM and DIC signal. Second, a more detailed analysis is conducted by comparing the FEM and DIC data considering two paths within the full-field maps. For both FOVs, all the kinematic variables are tracked one pixel below the interface (indicated with $\bar{x}_2$ in Fig. 4). This is an important aspect of the error quantification as it provides an estimate of the accuracy in measuring key quantities characterizing frictional ruptures, such as the slip and slip velocity, testing also the reliability of the data extrapolation provided by the "fill-boundary" algorithm. Another path is taken perpendicularly to the interface at a given coordinate $\bar{x}_1$, aimed to appraise the quality of the DIC measurement in resolving sharp and other peculiar features of the full-field structure. While the path plots along the interface are always extracted at $\bar{x}_1 = 0^-$ mm, the paths perpendicular to the interface are considered at different positions of interest depending on the spatiotemporal quantity analysed. Specifically, for the large FOV, we consider the position $\bar{x}_1 = 72.6$ mm, and, in the case of the small FOV, $\bar{x}_1 = 84.6$ mm for displacement and strain data, $\bar{x}_1 = 87$ mm for the particle velocity data.

Let us introduce a parameter that quantifies the choice of the DIC subset size with respect to the physical length-scale of the phenomenon. An important length-scale characterizing cracks is the size of the cohesive zone. Numerical studies on the spontaneous propagation of shear cracks along frictional interfaces often use an index to determine the resolution of the cohesive zone, defined as the ratio between the quasi-static length of the cohesive zone Λ^0 and

Table 2 DIC settings adopted in the virtual experiment analysis

Image resolution	400×250, 16-bit		
Image Acquisition Rate	2 million fps		
Fields of view	121×75.625 mm^2 – Large FOV,		
	19×11.875 mm^2 – Small FOV		
Pixel size	302.5 μm – Lage FOV ,		
	47.5 μm – Small FOV		
Patterning Technique	Matt white spray paint base coat with black dots		
Pattern feature size (approx.)	6.8 pixels		
DIC technique	2D correlation		
DIC software	Correlated Solution VIC-2D® 6, MatchID® 2020.1.1		
Matching criterion	Zero-normalised sum of square differences (ZNSSD)		
Image filtering	Gaussian, 5×5 pixel^2 kernel		
Subset shape function	Affine, Quadratic		
Interpolant	6-tap spline		
Strain formulation	Lagrangian		
Strain computation	Finite difference scheme		
Spatial smoothing	None		
Temporal smoothing	None		
		Large FOV	Small FOV
Subset size	11×11 pixel^2	3.33 mm	0.52 mm
	21×21 pixel^2	6.35 mm	1.00 mm
	31×31 pixel^2	9.38 mm	1.47 mm
	41×41 pixel^2	12.40 mm	1.95 mm
	51×51 pixel^2	15.43 mm	2.42 mm
Step size	1 pixel	302.5 μm	47.6 μm
Virtual Strain Gauge size	13 pixels	3.93 mm	0.62 mm
	23 pixels	6.96 mm	1.09 mm
	33 pixels	9.98 mm	1.57 mm
	43 pixels	13.01 mm	2.04 mm
	53 pixels	16.03 mm	2.52 mm

the element size [55, 65]. Here we use a similar approach for DIC measurements, introducing the cohesive length-to-subset size ratio $\lambda^0_{SB} = \Lambda^0/l_{SB}$. This dimensionless parameter characterizes the predicted resolution of the cohesive length obtained by the DIC measurement for the selected field of view. The details about the cohesive length Λ^0 are reported in Appendix 1; we use the expression for a rupture propagating with 0+ rupture speed, while the cohesive length associated with a higher rupture speed is generally smaller [1, 66]. Indeed, the representative actual cohesive zone length Λ^* in our FE simulations is smaller (Fig. 5; Table 3). However, similarly to [55], Λ^* can be seen as a relevant lengthscale for the cohesive zone length, known apriori if the friction law is known, which enables comparison and estimation of the performances of the subsets to resolve the full field structures associated with the rupture propagation. We also define the actual resolution of the cohesive zone by the subset as $\lambda^*_{SB} = \Lambda^*/l_{SB}$. The values of λ^0_{SB} and λ^*_{SB} for our modeling, computed for all subsets used, are listed in Table 3.

In the following sections, we report the DIC maps corresponding to the use of 11×11 pixel^2 subset for the large FOV and 41×41 pixel^2 subset for the small FOV, as they have similar sizes in the physical space and, therefore, offer a meaningful comparison of the DIC accuracy for different FOV. We also compare selected quantities for all subsets for the two FOVs. In previous experimental studies, a subset of 41×41 pixel^2 was used to process ultrahigh-speed images of supershear and sub-Rayleigh ruptures, e.g. [25, 26], as it provided the best compromise between spatial resolution and noise reduction in resolving the velocity and strain fields. Based on the resolution of the cohesive zone discussed above, one anticipates that, for the large FOV, the smallest subset of 11×11 pixel^2 may be capable of capturing most aspects of the sharp variations at the rupture tip, while the larger subsets would introduce averaging over scales comparable to or larger than the cohesive zone size, and hence should result in increasingly substantial smearing of the features. In contrast, for the small FOV, all subsets resolve the cohesive zone

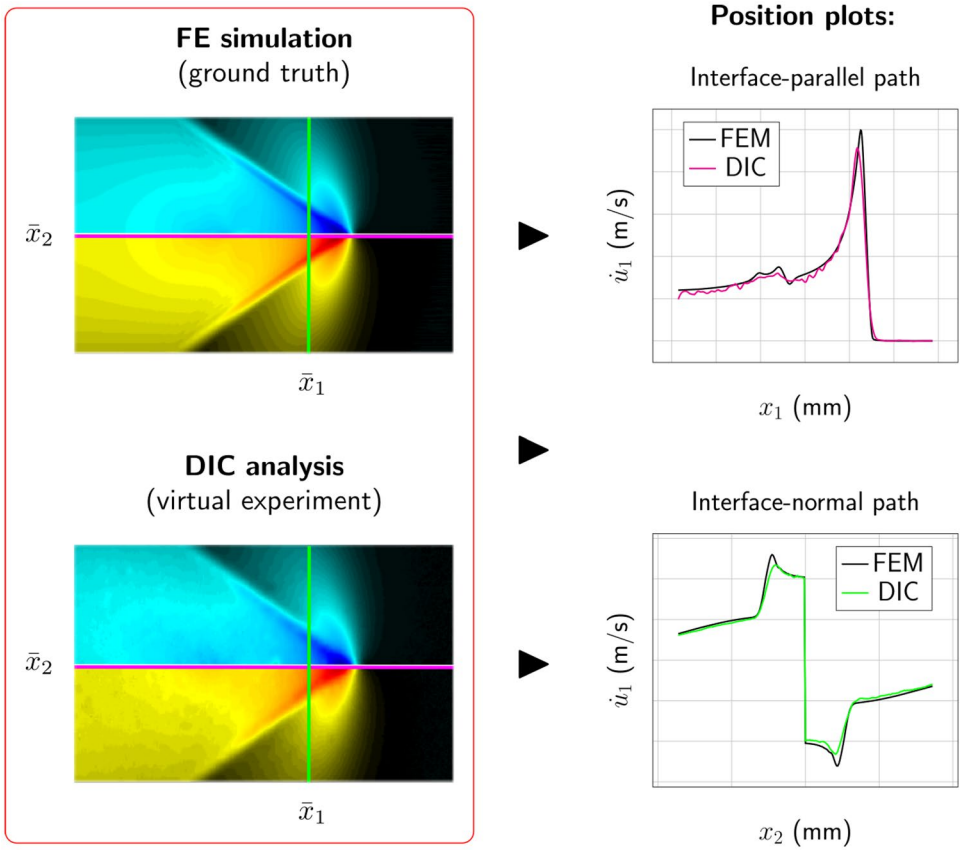

Fig. 4 Schematics of the analysis workflow employed in this study. Full-field DIC data are compared point-by-point with the ground-truth maps of the FEM simulation. The uncertainties related to the DIC measurement are also evaluated considering position paths parallel ($\bar{x}_2$) and perpendicular ($\bar{x}_1$) to the interface

length, although to a different degree, and one anticipates good results for all subset sizes used in our analysis. In fact, the 41×41 pixel^2 subset for the small FOV provides almost twice better resolution of the cohesive zone than the 11×11 pixel^2 subset for the large FOV.

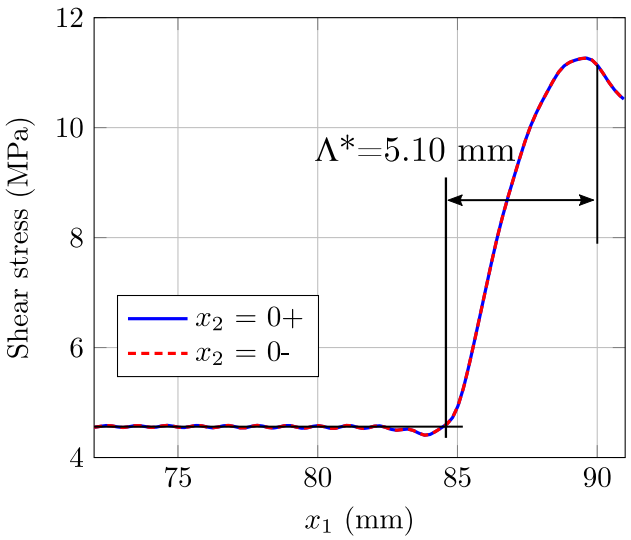

Fig. 5 Evaluation of the cohesive zone length Λ^* of the supershear rupture produced in the FE simulation. The cohesive length is identified as the distance over which shear stress decreases from its peak value to its dynamic value. The figure depicts the distribution of the shear stress along the interface at $t = 45.9$ μs

Characterization of the Displacement Uncertainties

A comparison of the interface-parallel displacement field u_1 obtained with the reference FEM simulation and the DIC analysis is shown in Fig. 6, for both large and small FOVs, at the time $t = 45.9$ μs after the rupture nucleation. Note that the displacement maps are cropped along the edges by 10 pixels, where DIC analysis is not performed, so that the DIC maps are slightly smaller compared to the finite element counterparts.

The interface-parallel displacement is characterized by the top plate moving in the leftward direction, and the bottom plate moving in the opposite direction, consistent with the shear motion of the dynamic rupture, for both FOVs considered. The DIC measurement is capable of capturing the anti-symmetric behaviour of u_1 with high fidelity, with the smaller subsets being noisier, as expected. To quantify the error measurement, we monitor the difference between FEM and DIC maps $\Delta u_1(x_1, x_2) = u_1^{\text{FEM}}(x_1, x_2) - u_1^{\text{DIC}}(x_1, x_2)$ (Fig. 6(e, f)). This analysis reveals that the displacement map produced by the large FOV attenuates the steep gradients in the near field of the Mach cone , while $\Delta u_1^{\max} \approx 6$ μm close to the interface behind the crack tip (Fig. 6(e)). The small

Table 3 Values of the estimated and simulated cohesive length to subset size ratio obtained for all subset sizes used to process images for both large and small FOVs. The table also reports the cohesive length in millimeters and in pixels according to the field of view dimension

	Λ^0		λ^0_{SB} according to subset size:				
	(pixel)	(mm)	11×11	21×21	31×31	41×41	51×51
Large FOV	32.14	9.72	2.92	1.53	1.04	0.78	0.63
Small FOV	204.67		18.61	9.75	6.60	4.99	4.01
	Λ^*		λ^*_{SB} according to subset size:				
	(pixel)	(mm)	11×11	21×21	31×31	41×41	51×51
Large FOV	16.86	5.10	1.53	0.80	0.54	0.41	0.33
Small FOV	107.37		9.76	5.11	3.46	2.62	2.11

FOV can better reconstruct the sharp features characterizing the Mach shock front, with the maximum error on the order of 1 μm (Fig. 6(f)). Note that both FOVs exhibit the same maximum error in pixels (0.025 pixels). However, this error becomes more detrimental for the large FOV as it is multiplied by the pixel size of 302.5 μm, while in the case of the small FOV it is multiplied by 47.6 μm.

A clearer interpretation about how the measurement uncertainty propagates between the two FOVs is given by displaying the error maps in percentage of the FEM signal at the same spatial locations (Fig. 6(g, h)). Moreover, to better locate the error distribution, we depict the contour lines of the FEM field overlapping the error maps. Panel (g) illustrates a magnified view of the large FOV using the window of the small FOV. The displacement data from the large FOV displays an error that exceeds -40% in front of the rupture tip and it goes up to 20% behind it. The higher error values are mostly distributed along the interface, where the displacement data are extrapolated by the DIC software. As for the large FOV, the highest error (more than 40% in absolute value) is concentrated in front of the rupture tip: here the displacement is relatively small ($< 1\mu$m from the contour plot), hence, it does not affect the overall quality of the field. Away from these regions, the discrepancy with the ground-truth FEM solution for the large FOV is around 7%. The small FOV (panel h) has a much smaller error, with an average error below 3% and the maximum error of about 10% near the rupture tip in the upper domain.

To further quantify the difference between the reference FEM and resulting DIC displacements, we trace u_1 along paths parallel ($x_2 = 0^-$ mm) and perpendicular ($x_1 = $ const.) to the interface. The paths perpendicular to the interface are traced at $x_1 = 72.6$ mm and $x_1 = 84.6$ mm for the large and small FOVs, respectively (Fig. 7). The plots of u_1 vs. x_1 show that the DIC measurements capture the steep rise of the interface-parallel displacement behind the rupture tip over a wide range of subset sizes (Fig. 7(a, b)). In the case of the large FOV, all subsets display a moderate attenuation of the u_1 signal affecting the reconstruction of the rapid increase of the displacement curve behind to the rupture tip. As previously discussed, the discrepancy between the FEM simulation and the measured data is around 6% at about 17.5 mm behind the rupture tip. The analysis on the small FOV exhibits a closer match between the DIC measurement and the FEM data, with an average error along the interface around 2.8%. Similarly,the plots of u_1 vs. x_2 reveal a moderate attenuation of the displacement jump across the interface in case of the large FOV (of 3.8 μm), and only a slight attenuation in the case of small FOV (1.2 μm) (Fig. 7(c, d)). Note that Fig. 7(c) and (d) are plotted on a different scale. The higher reduction of displacement jump in the case of large FOV is likely due to low spatial resolution of field gradients closer to the interface. Note that the agreement between DIC measurement and FEM displacements is consistently good across a range of subset sizes, indicating that even the intrinsic smoothing associated with the 41×41 pixel^2 subset does not change the shape of the interface-parallel displacement field.

The comparison between the reference FEM simulations and the corresponding DIC measurements of the interface-normal displacement u_2 is presented in Figs. 8 and 9. For the large FOV, the FEM map of the interface-normal displacement displays a symmetric pattern with respect to the interface, as expected, and it is characterized by an upward movement of almost 4.3 μm near the rupture tip followed by a downward motion up to -20 μm (Fig. 8(a)). The upward motion is comparatively smaller and it localized at the rupture tip. Hence, it is better described by adopting a magnified view of the the finite element simulations around the rupture tip (Fig. 8(b)), motivating the employment of a small FOV when analyzing this feature with the DIC analysis. The DIC measurements are indeed capable of capturing these features (Fig. 8(c, d)). Zooming in on the large FOV, we can compare the error in resolving the complex structure near to rupture tip between the two FOV (Fig. 8(g, h)). Here, even by using the 11×11 pixel^2 subset, the upward motion is attenuated by about 30%, while a large portion of the transition zone behind the crack tip, where the displacement field goes from

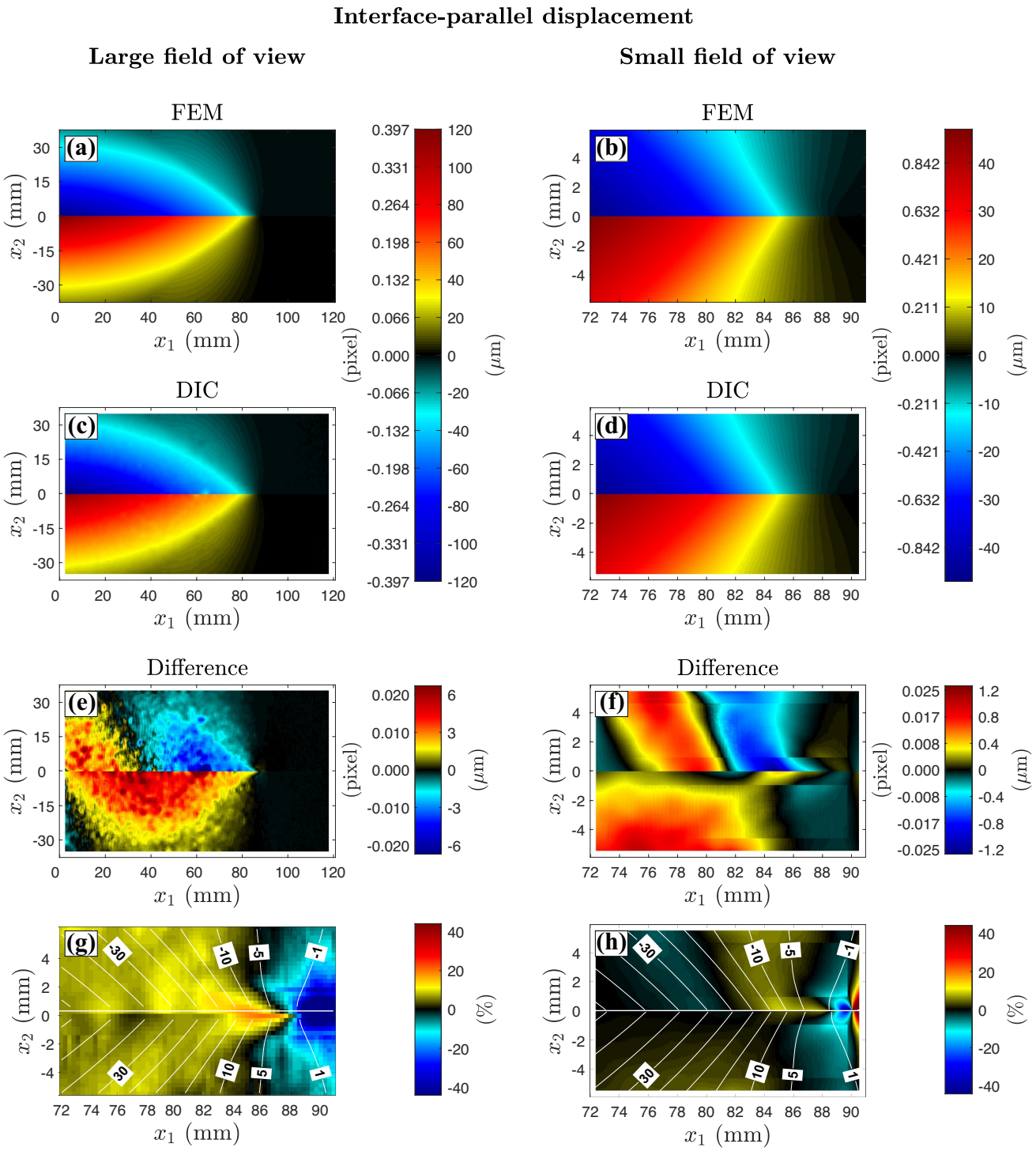

Fig. 6 Interface-parallel displacement for the two fields of view at $t = 45.9$ μs. Full-field maps obtained from the (**a**, **b**) FEM simulations and (**c**, **d**) DIC analysis. The subset size employed in the correlation is of 11×11 pixel^2 for the large FOV and 41×41 pixel^2 for the small FOV. Evaluation of the DIC error: (**e**, **f**) difference between FEM and DIC data, (**g**, **h**) error in percentage of the actual (FEM) value, zooming in on the large FOV to the same locations as the small FOV. The white contours indicate the isoline of the FEM signal taken every 5 μm

-2 μm to 2 μm in a few points, exceeds 70% of error. The small FOV offers a much smaller percentage error, with only a slender distribution of points showing large error values; next to the interface, the overall error decreases to less than the 4%. A closer look at the contour plots further reveals that the locations of the largest errors corresponds to data

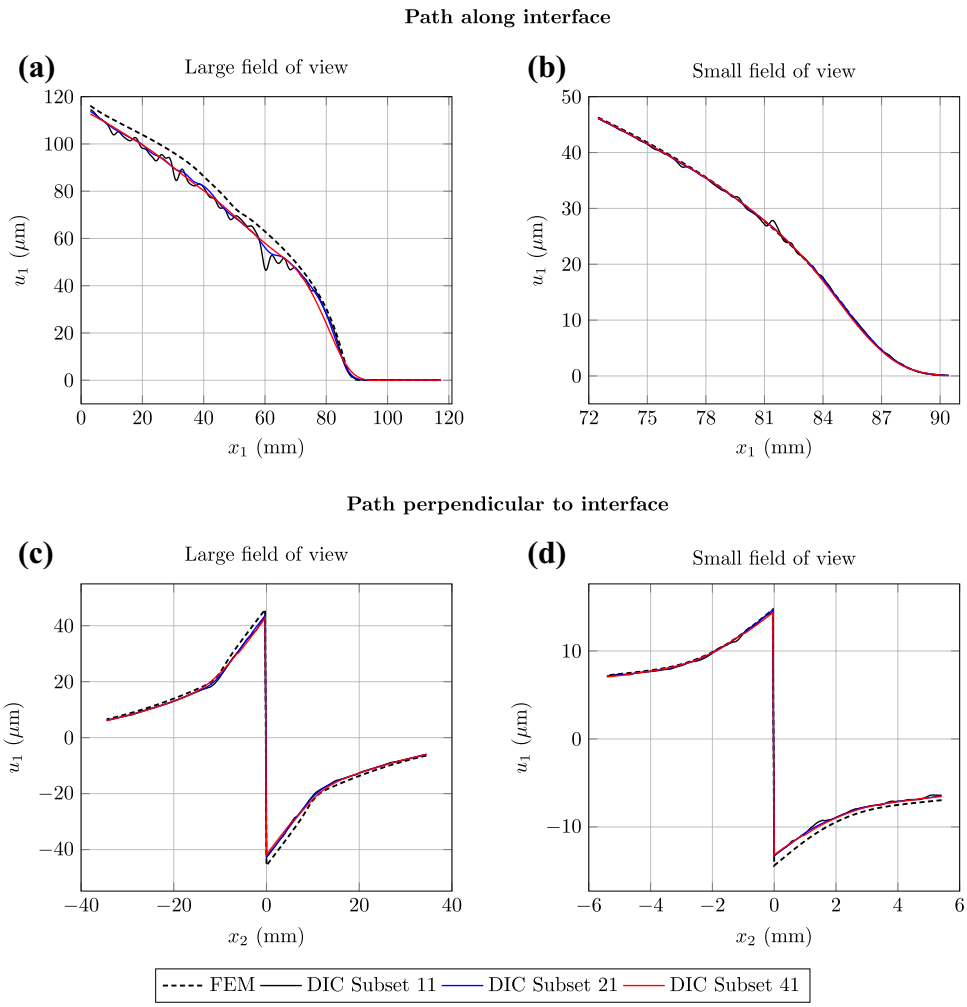

Fig. 7 Interface-parallel displacement vs. position along (**a**, **b**) and perpendicular (**c**, **d**) the interface at $t = 45.9\ \mu$s for the large (left) and small (right) fields of view. The plots compare the reference FEM simulations with the DIC analysis performed with different subset sizes

points where actual u_2 is almost zero, which makes the error calculation particularly sensitive to differences that can be considered negligible. Therefore, the points with 70% of error reflect locations with near-zero values of the underlying signal, and the measured maps match all the structure characteristics from the numerical simulation well.

To study the effect of the subset size on the reconstruction of the interface-normal field, we track u_2 vs x_1 and x_2 (Fig 9). In the case of the large FOV, these plots show how the DIC measurement obtained with a subset size of 11×11 pixel^2 does a better job in reconstructing the positive upward peak of u_2 compared to the subset size of 41×41 pixel^2. All subset sizes used overestimate the subsequent negative peak (Fig. 9(a)). The plot of u_2 vs x_2 shows the ability of the DIC measurement to capture the sharp gradients of the displacement field associated with the formation of shear Mach cone (Fig. 9(c)). The Mach cone features result in two negative peaks at $x_2 = \pm 11.8$ mm; the plot Fig. 9(c) shows the influence of the subset size in measuring such peaks. The error associated for the reconstruction of the $-7.5\ \mu$m peaks is about 4.3% and 14.5% for the 11×11 and 41×41 pixel^2 subset data, respectively. In the case of the small FOV, the larger subset size (41×41 pixel^2) shows a better agreement with the FEM reference, filtering out the noise produced by smaller subsets and enhancing the overall quality of the signal (Fig. 9(b–d)).

In Fig. 9(a, b), we can observe opposite effects of the subset size: on the one hand, the large FOV benefits from a smaller subset, which helps to resolve the sharp features of the field; on the other hand, the small FOV obtains better results using a bigger subset. The DIC process acts as non-linear filter whose impact depends from the correlation settings and the way they interacts with the signal characteristics [35]. This mainly results in a smoothing effect of the signal, complemented by the production of artifacts in the measured field. Therefore, since the main issue of the large FOV concerns the spatial resolution of sharp structures, the higher smoothing effect performed by a bigger subset has a predominant role in driving the measurement accuracy. Indeed, according to Table 3, the smallest subset size of 11×11 pixel^2 is smaller than the actual, simulated cohesive zone size, allowing for resolution of the sharp features at the rupture front, while the

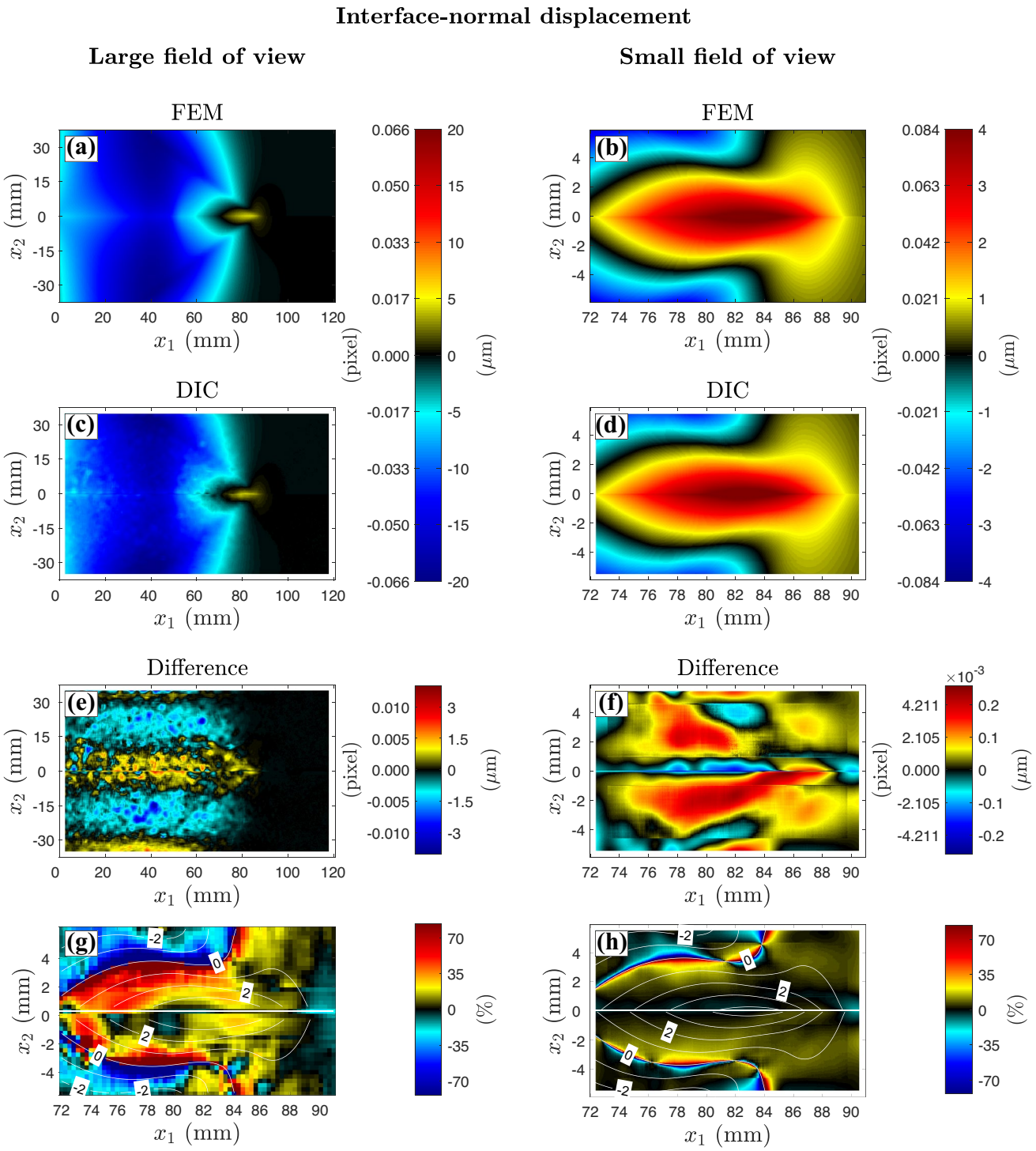

Fig. 8 Interface-normal displacement for the two fields of view at $t = 45.9\ \mu$s. Full-field maps obtained from the (**a**, **b**) FEM simulations and (**c**, **d**) DIC analysis. The subset size employed in the correlation is of 11×11 pixel^2 for the large FOV and 41×41 pixel^2 for the small FOV. Evaluation of the DIC error: (**e**, **f**) difference between FEM and DIC data, (**g**, **h**) error in percentage of the actual(FEM) values, zooming in on the large FOV to the same locations as the small FOV. The white contours indicate the isoline of the FEM signal taken every 1 μm

larger subsets are comparable to or larger than the cohesive zone size, resulting in too much averaging. On the other hand, the enhanced spatial resolution offered by the small FOV makes all subset sizes significantly smaller than the cohesive zone size, allowing to resolve it in principle, and the measured signal is more sensitive to numerical artifacts generated by the

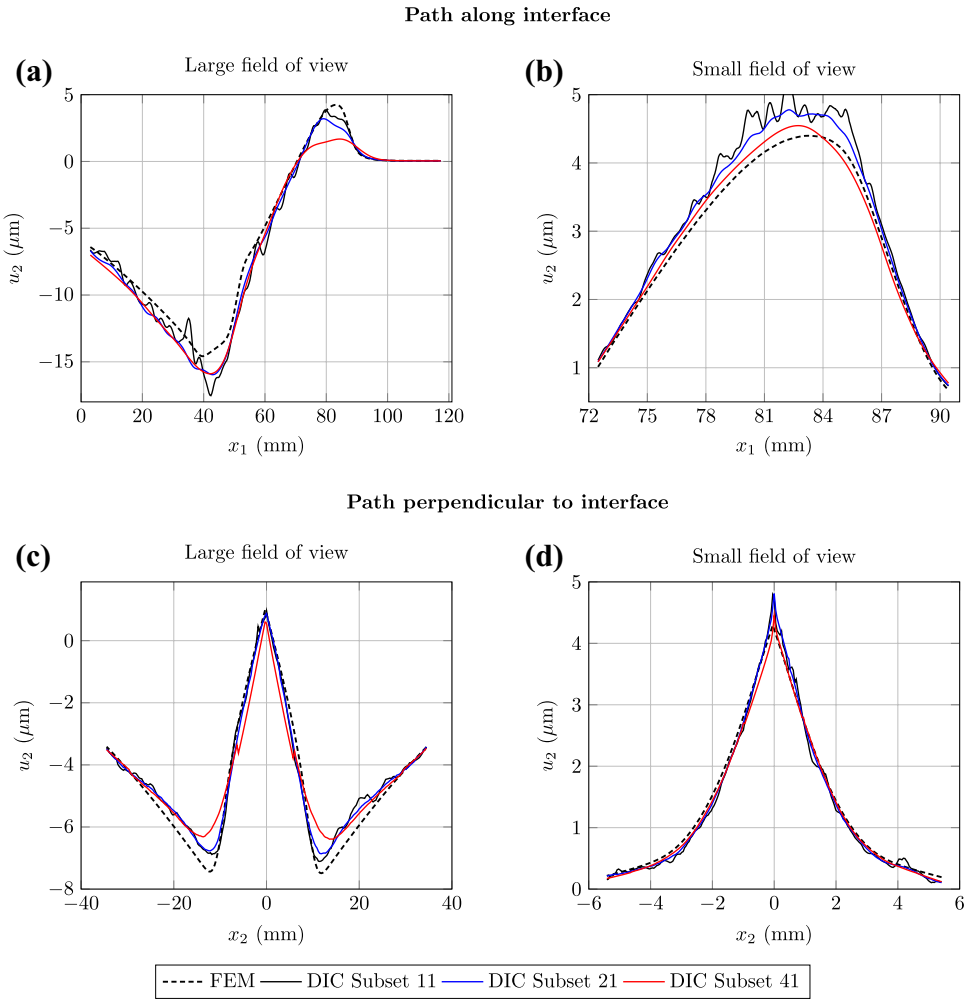

Fig. 9 Interface-normal displacement vs. position along (**a**, **b**) and perpendicular (**c**, **d**) the interface at $t = 45.9\ \mu$s for the large (left) and small (right) fields of view. The plots compare the reference FEM simulations with the DIC analysis performed with different subset sizes

correlation process, which, in contrast, are better tackled by increasing the subset size.

A further comparison is depicted in Fig. 10, where the displacement signals are displayed for the two fields of view among the same physical window close to the rupture tip. The data are sampled along a path perpendicular to the interface at the same horizontal coordinate ($x_1 = 84.6$ mm), reporting the measurement obtained with subsets having similar dimensions in the physical space. Note that reference FEM curves are slightly different between the large and small fields of view due to the different grid pitch used for the interpolation of the nodal displacement values.

While the small FOV provides a reliable identification of the displacement signal, the curves obtained from the large FOV show a loss of accuracy within half-subset away from the interface. We can deduce that the subset size does not provide enough resolution to perfectly match the displacement gradient spanning over few pixels from the interface. In turn, such uncertainty spreads to the interface due to extrapolation made by the correlation algorithm.

Full-field Particle Velocity Uncertainties

The comparison between the reference FEM simulations and DIC analysis of the particle velocities $\dot{u}_1$ and $\dot{u}_2$, in the interface-parallel and interface-normal directions, are given at the timestep $t = 45.9\ \mu$s in Figs. 11, 12, 14, and 15, respectively. The full-field map of the particle velocity component $\dot{u}_1$ produced by the FEM simulations for the large FOV shows two main features: (i) the development of shock front features, associated with the supershear propagation of the crack, and (ii) the formation of two anti-symmetric lobes around the rupture tip, associated with the dilatational field (Fig. 11(a)), as expected from theoretical and experimental observations of supershear ruptures (e.g. [1, 16, 25, 29, 51]). The supershear nature of the rupture is also confirmed by tracking the crack tip along the interface, which reveals a propagation speed of $V_r = 2.18$ km/s, and a ratio of the rupture speed-to-shear wave speed of $V_r/c_s = 1.66$, where $c_s = 1.28$ km/s is the shear wave speed of the material. While there are striking similarities between the particle velocity maps of the present simulations and those of prior experiments [16, 25, 29],

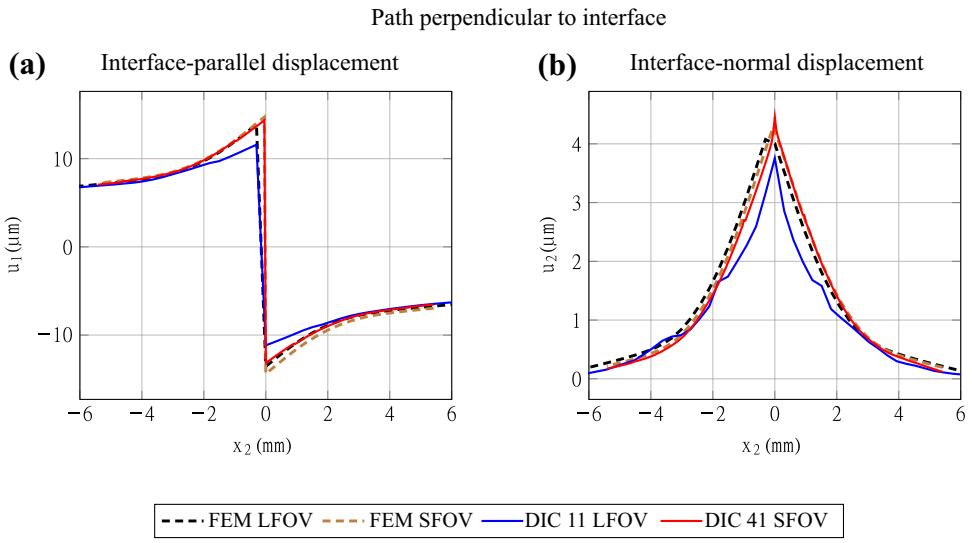

Fig. 10 Displacement signals vs. position on a path perpendicular to the interface at $x_1 = 84.6$ mm and $t = 45.9$ μs: comparison between the small and the large field of view using 11×11 pixel^2 and 41×41 pixel^2 subsets, respectively

there are also significant, qualitative differences. One of the most prominent differences is the formation, in the laboratory experiments, of an additional set of shock fronts associated with the dilatational field, resulting in pressure Mach features [29]. The formation of such additional shock features has been attributed to the strain-rate-dependent behavior of the polymers used in the experiments [29]. Another important difference is that both the shear and pressure features exhibited by prior experimental measurements are blunter compared to the present numerical simulations. Note that these prior experimental measurements of the particle velocities have been compared with independent measurements obtained with laser velocimeters, showing excellent agreement. Hence, the qualitative differences between these prior measurements and the present simulations are likely due to the simplified constitutive laws assumed in the finite element model, featuring effective linear elastic properties (see "Finite Element Model of the Laboratory Experiments" section). In the current work, we explore the ability of DIC to capture sharper (and more challenging to capture) features than expected in viscoelastic materials used in prior tests. In future studies, we plan to include viscoelastic material properties, capturing the highly strain-rate dependent behavior displayed by these polymers.

In the case of the large FOV, the DIC measurement resulting from the analysis of the numerically deformed images with the 11×11 pixel^2 subset do capture the main structure of the interface-parallel velocity field $\dot{u}_1$, despite showing a moderate attenuation of sharpest gradients (Fig. 11(c–e)). For example, the particle velocity around the shock fronts exceeds 8 m/s (in absolute value), while the measurement blunts the sharp features associated with the shear Mach cone, locally decreasing the magnitude of the velocity field by almost 0.6 m/s, due to the smoothing effect provided by the subset. The highest depletion of signal is observed close to the rupture tip, where few measurement points are characterized by a reduction of velocity of almost 2 m/s. In terms of percentage error (Fig. 11(g)), the particle velocity is reduced by 15% on the sharp feature marking the Mach cone, whose difference becomes around 25% on the interface. The error outstrips 40% (in modulus) in front of the rupture tip where there the velocity signal presents a steep gradient from 0 to 2 m/s. As in the case of the interface-parallel displacement, this localized error distribution affects measurement points where the velocity signal is relatively small, and does not significantly modify the field structure.

The loss of information associated with the larger subset sizes is highlighted by plotting $\dot{u}_1$ vs. x_1 (at $x_2 = 0^-$) (Fig. 12(a)). This plot shows that increasing the subset size up to 41×41 pixel^2 significantly weakens the peak velocity. Another effect is that larger subset sizes tend to anticipate the rise of particle velocity ahead of the rupture tip and to modify the position of the velocity peak. These results indicate that, to adequately resolve the rapidly evolving fields at the rupture tip, it is important to choose the subset size sufficiently smaller than the cohesive zone size. Note that the results are obtained in an ideal setting of noiseless images. Therefore, while this numerical analysis suggests that the smallest subset performs best in the absence of noise, such a small subset size used with noisy experimental images has been shown not to be able to adequately resolve the spatial features of dynamic ruptures (e.g. Fig. 14(a) in [25]). The dual goals of resolving well the features of the rupture front and combat noise would thus place limitations on how large the field of view can be.

To better characterize the ability of the DIC measurement to describe the shock features, we track the interface-parallel velocity field $\dot{u}_1$ along a vertical path at $x_2 = 72.6$ mm (Fig. 12(c)). The spatial resolution of the largest subset used in this analysis cannot resolve this sharp gradient, displaying a monotonic trend moving away from the interface. By contrast, the $\dot{u}_1$ profile produced with a subset size of 11×11 pixel^2 (and 21×21 pixel^2,

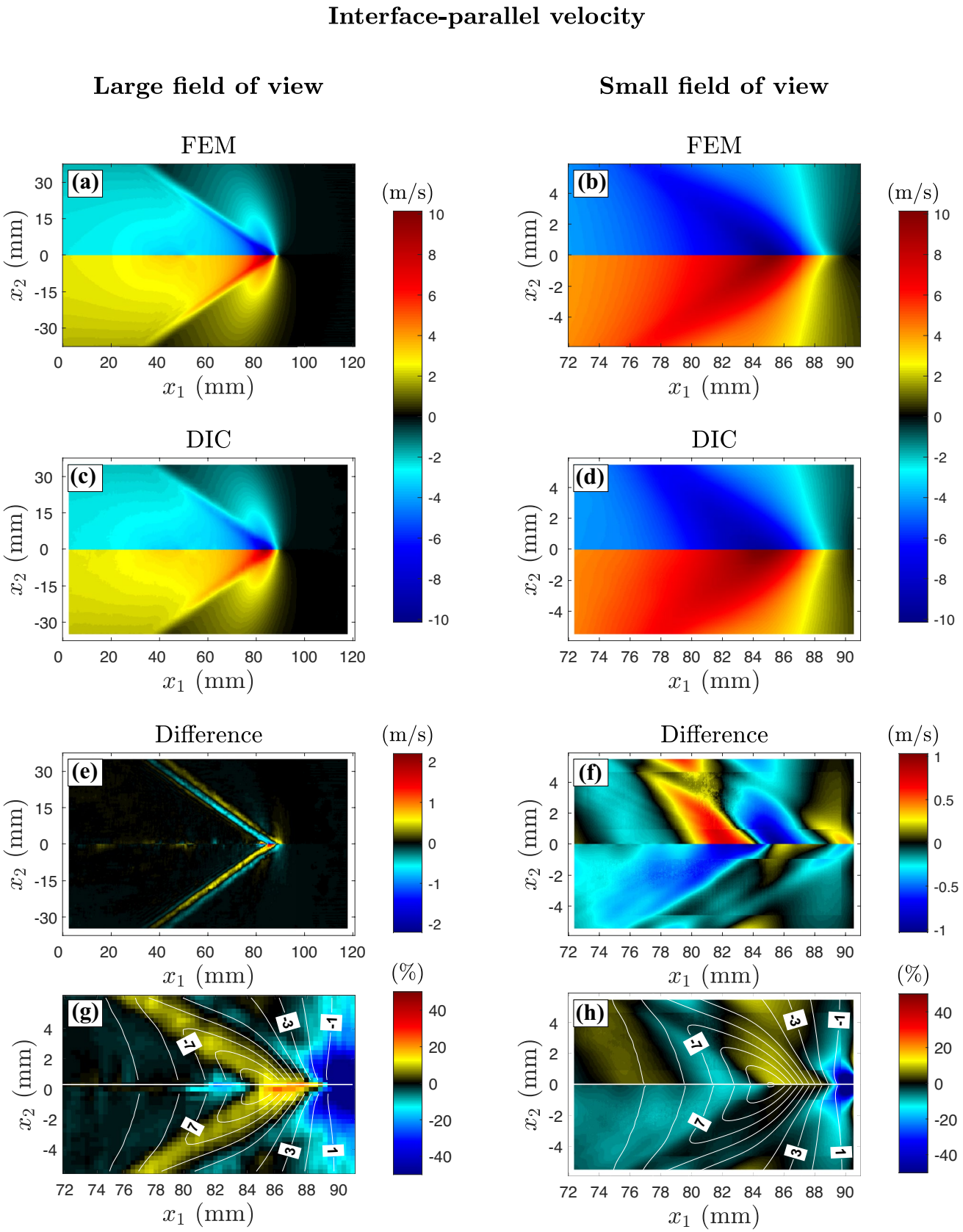
Interface-parallel velocity
Large field of view
Small field of view
FEM
DIC
Difference
(a)
(b)
(c)
(d)
(e)
(f)
(g)
(h)
x_1 (mm)
x_2 (mm)
(m/s)
(%)

◂**Fig. 11** Interface-parallel particle velocity for the two fields of view at $t = 45.9$ μs. Full-field maps obtained from the (**a**, **b**) FEM simulations and (**c**, **d**) DIC analysis. The DIC measurements are performed using a subset size of 11×11 pixel^2 for the large FOV and 41×41 pixel^2 for the small FOV. Evaluation of the DIC error: (**e**, **f**) difference between FEM and DIC data, (**g**, **h**) error in percentage of the actual (FEM) values, zooming in on the large FOV to the same locations as the small FOV. The white contours indicate the isoline of the FEM signal taken every 1 m/s

to a lesser degree) reasonably describes such features, without showing a strong increase in noise.

In the case of the small FOV, the interface-parallel velocity field $\dot{u}_1$ closely reproduces the FEM reference simulation using the 41×41 pixel^2 subset (Fig. 11(f)), with the absolute error below 1 m/s and mostly located close to the interface. Most of the measurement points displays absolute values of error below 10% (Fig. 11(h)). However, the upper domain presents three oscillating bands which are absent in the lower domain. A similar pattern can be also found in the error maps of u_1 (Fig. 6(f–h)), and, as previously mentioned, can be ascribed to the non-linear filtering effect induced by the correlation algorithm. These artifacts on the displacement field, which propagates though the temporal and spatial derivation, are intrinsic to the DIC analysis and arise from the complex interaction between the correlation settings (the subset transformation function, the sub-pixel interpolation, the gray-level range, the adopted speckle pattern, etc.) and the field signal [35]. This can be verified by comparing, for instance, the error pattern and $\dot{u}_1$ maps from another DIC software (see "Effect of the Order of Subset Transformation Functions" section), which produce slightly different outcomes even with the same correlation settings. Nonetheless, the error is relatively small for the small FOV and the DIC measurement offers a close reconstruction of the velocity field.

Concerning the effect of the subset size for the small FOV, the use of a smaller subset (i.e. 11×11 pixel^2) produces a markedly nosier signal and no benefits for the correlation (Fig. 12(b)). This is because all the subset sizes considered adequately resolve the cohesive zone size, with no excessive

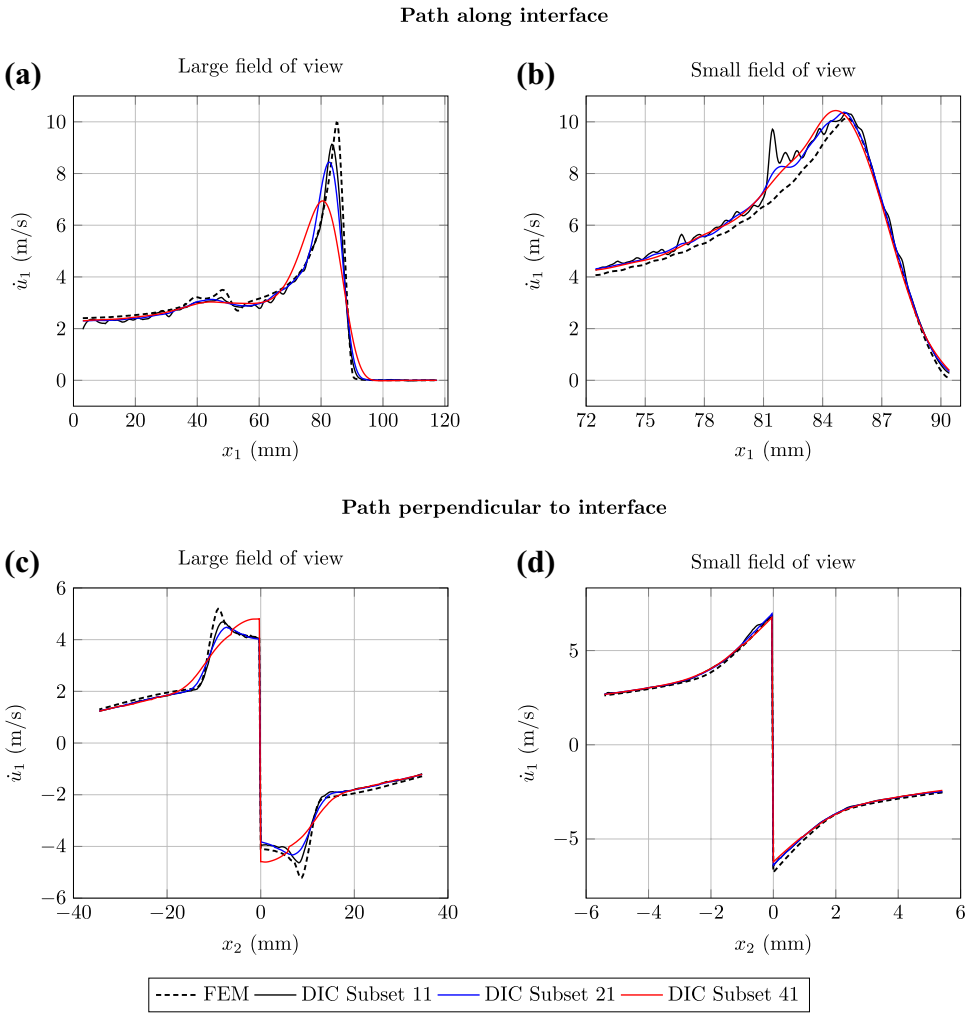

Fig. 12 Interface-parallel particle velocity vs. position (**a**, **b**) along and (**c**, **d**) perpendicular to the interface at $t = 45.9$ μs for the large (left) and small (right) fields of view. The plots compare the FEM simulations with the DIC analysis using various subset sizes

averaging. Due to the characteristic length scale of the velocity features in the small FOV being several pixels across, the 41×41 pixel^2 subset offers a good compromise between spatial resolution and noise mitigation. This observation is also confirmed by comparing the velocity values on a path perpendicular to the interface at $x_1 = 87$ mm (Fig. 12(d)).

To quantify the DIC measurement error, we track the amplitude and position of the particle velocity $\dot{u}_1$ peak as a function of the subset size. As already discussed, larger subsets degrade the particle velocity signal if they do not adequately resolve the cohesive zone size. In particular, the DIC underestimates the velocity peak in the large FOV with respect to the FEM simulation, resulting in an increase of the error from the 8.4% for the 11×11 pixel^2 subset up to 36% by using the 51×51 pixel^2 subset (Fig. 13(a)). In the case of the small FOV, all subsets resolve the cohesive zone size, although the largest subset has a marginal resolution of 2, and the DIC analysis generally captures well both the magnitude and location of the peak. Looking in more detail, the DIC with a small FOV slightly overestimates the velocity peak with respect to the FEM, increasing the error from 1.97% to 3.1%. Note that the reference signal of the interface-parallel velocity peak is slightly different between the two FOV, although the virtual experiment is performed starting from the same numerical simulation. Again, such deviation is related to the interpolation of FEM nodal variables on a regular grid, which is generated a quarter of pixel far from the interface in order to avoid numerical errors during the interpolation process. The identification of the velocity-peak position is also influenced by the smoothing effect of the subset (Fig. 13(b)); for both FOVs, the DIC measurement locates the peak generally closer to the rupture initiation location compared to the numerical simulation, due to smoothing, exhibiting a difference from 1.8% (1.51 mm) to 6.8% (5.75 mm) for the Large FOV, and from 0.4% (0.05 mm) to 0.84% (0.71 mm) for the small FOV. Again, DIC with the small FOV matches the location of the peak quite well for all subsets considered.

Fig. 14 Interface-normal particle velocity for the two fields of view at $t = 45.9$ μs. Full-field maps obtained from the (**a**, **b**) FEM simulations and (**c**, **d**) DIC measurements. The DIC analysis uses a subset size of 11×11 pixel^2 for the large FOV and 41×41 pixel^2 for the small FOV. Evaluation of the DIC error: (**e**, **f**) difference between FEM and DIC data, (**g**, **h**) error in percentage of the actual(FEM) values, zooming in of the large FOV to the same locations of the small FOV. The white contours indicate the isoline of the FEM signal taken every 0.5 m/s

The interface-normal velocity $\dot{u}_2$ map produced by the FEM analysis for the large FOV presents a pattern of negative motion symmetric with respect to the interface. A small region of positive motion (Fig. 14(a)) delineates the shear Mach cone, consistent with theoretical predictions [67]. Another characteristic feature displayed by the interface-normal velocity is a region with negative motion, behind the rupture tip, exhibiting the typical peanut-like structure of a trailing-Rayleigh signature (e.g. [26, 67]). In the case of the large FOV, the correlation with 11×11 pixel^2 subset, while capturing the large-scale features of the velocity structure, does miss some of the sharp features mentioned above (Fig. 8(c–e–g)), namely the two positive wedges of 0.5 m/s, corresponding to the Mach cone. The small length-scale of such features, which is less than 7 pixels from the interface, makes the measurement particularly sensitive to the subset size. This is emphasized by plotting $\dot{u}_2$ vs. x_1 and x_2 (Fig. 15(a–c)). In particular, these plots show that, while the virtual measurements produced with a subset size of 41×41 pixel^2 can capture the positive peak at the rupture tip (though attenuated by more than 70%) (Fig. 15(a)), the smoothing effect produced by this large subset size, which has length much larger than the cohesive zone length, levels off the steep peaks of velocity of the Mach front (Fig. 15(c)).

Full-field measurements using the small FOV offer a magnified view of the interface-normal velocity field in the near-field of the rupture tip (Fig. 14(b)). Since the small FOV increases the number of pixels covering the velocity features, the DIC analysis performed with the 41×41 pixel^2

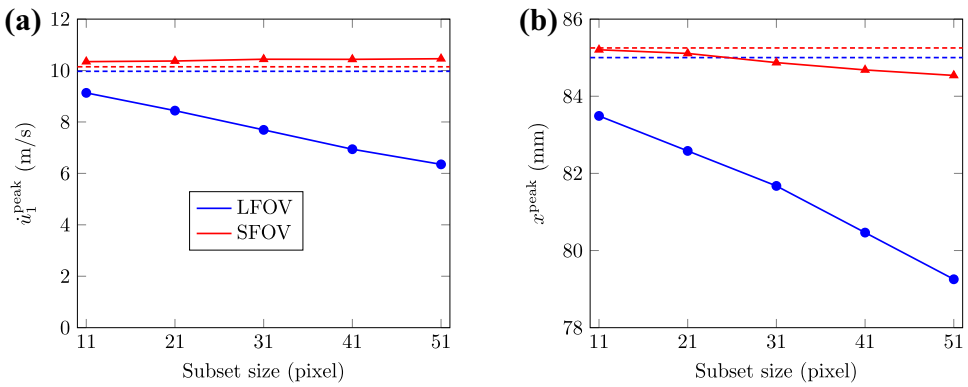

Fig. 13 Influence of the subset size in detecting the interface-parallel velocity peak in terms of its magnitude (**a**) and position (**b**). The blue and red curves indicates the large and small FOVs respectively; the dashed lines represents the FEM reference values

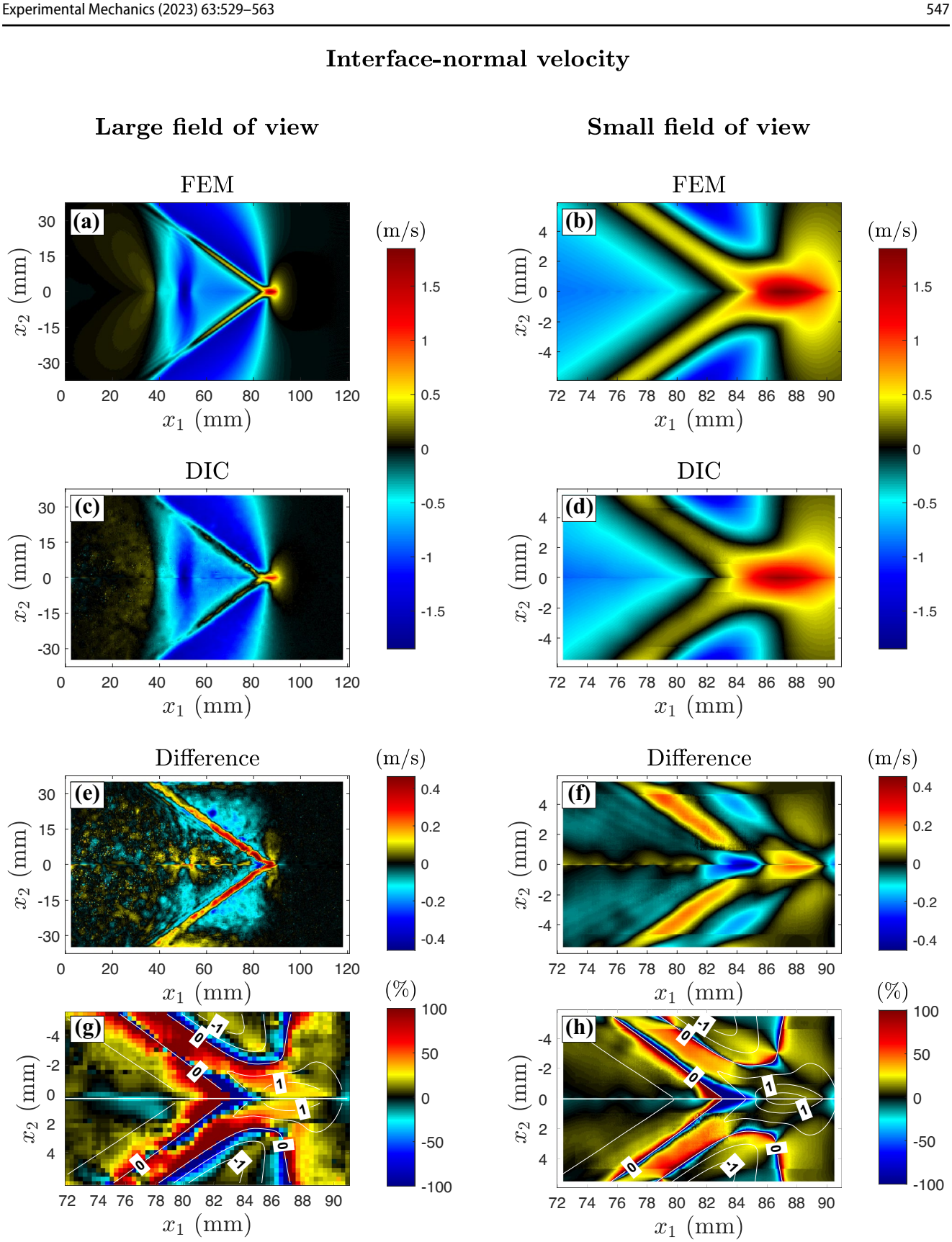
Interface-normal velocity
Large field of view
Small field of view
FEM
DIC
Difference
(a)
(b)
(c)
(d)
(e)
(f)
(g)
(h)
(m/s)
(%)
x_1 (mm)
x_2 (mm)

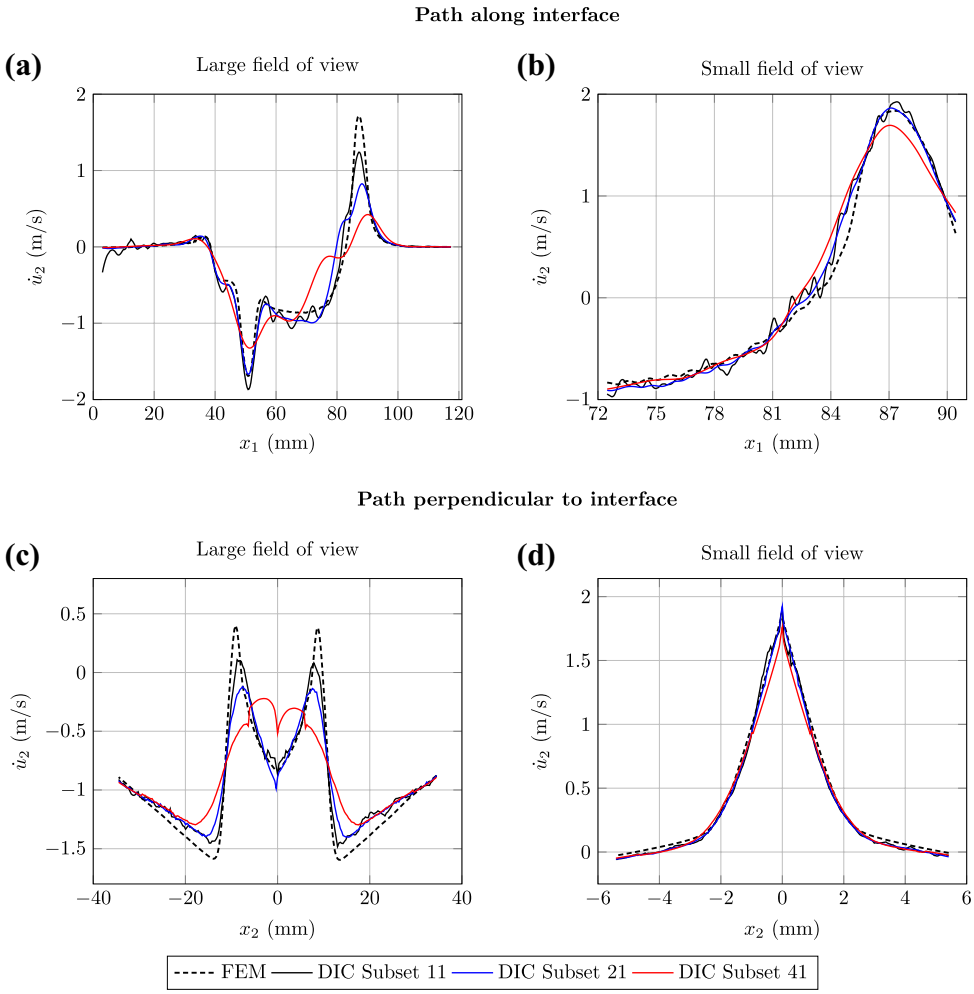

Fig. 15 Interface-normal particle velocity vs. position (**a**, **b**) along and (**c**, **d**) perpendicular to the interface at $t = 45.9$ μs for large (left) and small (right) fields of view. The plots compare the FEM simulations with the DIC measurements for different subset sizes

subset is capable of capturing the positive motion at the rupture tip and the sharp features associated with the supershear nature of the rupture. At the same time, the virtual measurements attenuate part of the sharp features formed by the supershear rupture (Fig. 14(d–f–h)). In particular, the map of the error in percentage highlights the data points more affected by the DIC uncertainties: as expected, the bias is higher where the velocity field is near zero, as it transitions from positive to negative values around $\dot{u}_2 = 0$. While this sharp transition is reasonably reconstructed by the DIC measurement, the positive wedges are mitigated by almost 40%. Quantitatively this error corresponds to almost 0.4 m/s for the 41×41 pixel^2 subset. On the interface, the positive lobe is well captured, and the difference with respect to the ground-truth is around 10% where the interface-normal velocity reaches its maximum (1.5 m/s). This discrepancy between the FEM and DIC data can be mitigated by employing a smaller subset (i.e. 11×11 pixel^2 or even 21×21 pixel^2), at the cost of an increased noise in the velocity signal (Fig. 15(b–d)).

The comparison of the particle velocity signals sampled along a path perpendicular to the interface at the same location for both the FOVs (Fig. 16) shows similar conclusions as observed in Fig. 10. The small FOV matches the reference signal from the FEM simulation; on the other hand, the large FOV differs from the ground-truth over half-subset distance from the interface. Such degradation of the signal in the velocity components also demonstrates the lack of accuracy in resolving fine features from the large FOV due to the reduced spatial resolution.

The evaluation of the DIC error in resolving the particle velocity fields gives also a quantitative perception of the subset's capability to capture all the features of the field structures, pointing towards the identification of simple practical rules for choosing the optimal analysis settings. In this sense, the analysis on the two fields of view offers a wide span of cases where the characteristic length-scale of the evolving supershear crack is related to the DIC spatial resolution, as indicated by the cohesive length-to-subset size ratio λ^*_{SB}. Since the large FOV represents a challenging configuration

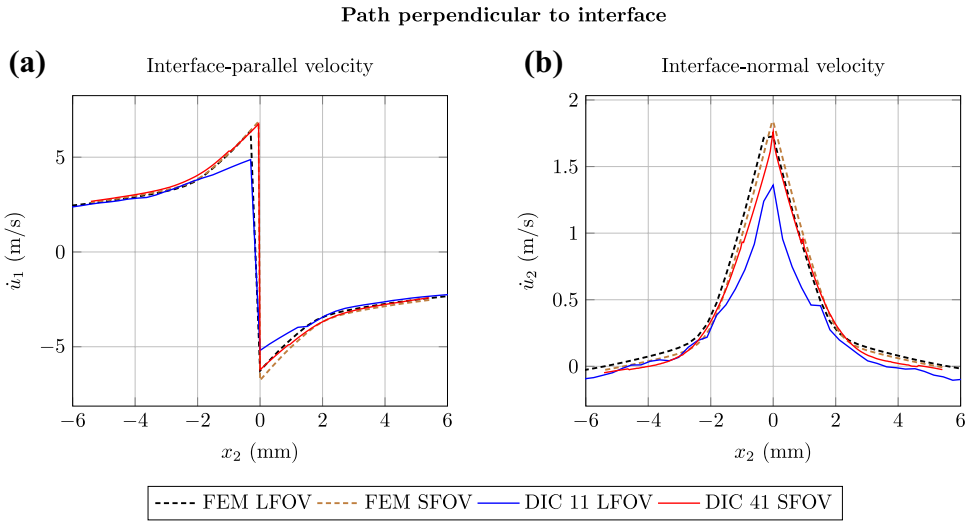

Fig. 16 Particle velocity signals vs. position on a path perpendicular to the interface at $x_1 = 87$ mm and $t = 45.9$ μs: comparison between the small and the large field of view using 11×11 pixel^2 and 41×41 pixel^2 subset, respectively

for the DIC analysis, we can deduce that correlations performed with $\lambda^*_{SB} > 1.5$ allows to distinguish in detail the sharp features of the interface-parallel velocity field. Notwithstanding, the λ^*_{SB} should be increased to detect the sharp positive concentrations in the interface-normal velocity structure, using, for instance, a magnified field of view.

Full-field Strain Uncertainties

To emphasize the strain changes associated with the propagation of the dynamic rupture, we compute strains with respect to the deformed condition just before the arrival of dynamic rupture (Figs. 17, 18, 19, and 20).

For the large FOV, the interface-parallel strain ε_{11} is characterized by an anti-symmetric structure featuring a tensile (compressive) strain in the top (bottom) plate, reaching a maximum strain level of 0.0045 ε at the rupture tip (Fig. 17(a)). If the dynamic rupture is propagating in steady-state conditions, the interface-parallel strain field is related to the interface-parallel velocity $\dot{u}_1$, by the equation $\varepsilon_{11} = -\dot{u}_1/V_r$, where V_r indicates the rupture speed. Our rupture is close to that condition. Similarly to the particle velocity component $\dot{u}_1$, the interface-parallel strain structure is also characterized by sharp features associated with the Mach cone. These features can be detected only by using a reduced subset size. However, the numerical differentiation process involved in the strain computation strongly amplifies the noise contained in the displacement signal, resulting in noisy strain maps, particularly in the case of the 11×11 pixel^2 subset (Fig. 17(d)). The impact of the subset size can be observed by tracking the strain data along paths parallel and perpendicular to the interface, as reported in Fig. 18(a, b). The smoothing effect related to a larger subset size has a predominant role for enhancing the quality of the interface-parallel strain data, but the reduced measurement resolution underestimates, for instance, the strain concentration at the rupture tip by up to 46% (Fig. 18(a)) and misses the sharp strain concentrations associated with the Mach cone (Fig. 18(b)).

Similarly, the sharp features exhibited by the interface-normal strain ε_{22} are captured by the 11×11 pixel^2 subset, at the cost of high noise levels (Fig. 17(e–h)). A closer analysis of the interface-normal strain signal sampled one pixel below the interface (Fig. 18(c)) reveals that the raw DIC data from the large FOV yield negative values of interface-normal strain independently from the subset size; in this case, the 21×21 pixel^2 subset helps to reduce the noise and to have a good description of the ε_{22} positive peak on the rupture tip. However, the correction of the negative drop requires the use of a further filtering procedure, not discussed here.

The DIC measurement performed with the 11×11 pixel^2 subset allows us to identify the shear Mach cone structure displayed by the shear strain field ε_{12}, as well as to reproduce the localized negative shear strain zone ahead of the rupture tip reaching $\approx$−0.0005 ε (Fig. 17(c–f)). The shear strain concentration ahead of the rupture tip can be observed in detail by plotting the shear stain along the interface (Fig. 18(e)), where the 11×11 pixel^2 subset measures with good accuracy the rapid rise of the strain signal beyond at the rupture tip. After this initial peak the shear strain evolves to a constant level. However, none of the used subsets is capable of replicating the constant trend at 0.0013 ε. A closer analysis on the position plots along path perpendicular to the interface (Fig. 18(f)), shows that increasing the subset size leads to suppressing the sharp ε_{12} concentration of the supershear shock front and to reducing the strain magnitude inside the Mach cone.

The DIC measurements obtained with the small FOV provide an accurate reconstruction of the strain fields even by using the 41×41 pixel^2 subset (Fig. 19). The structure of

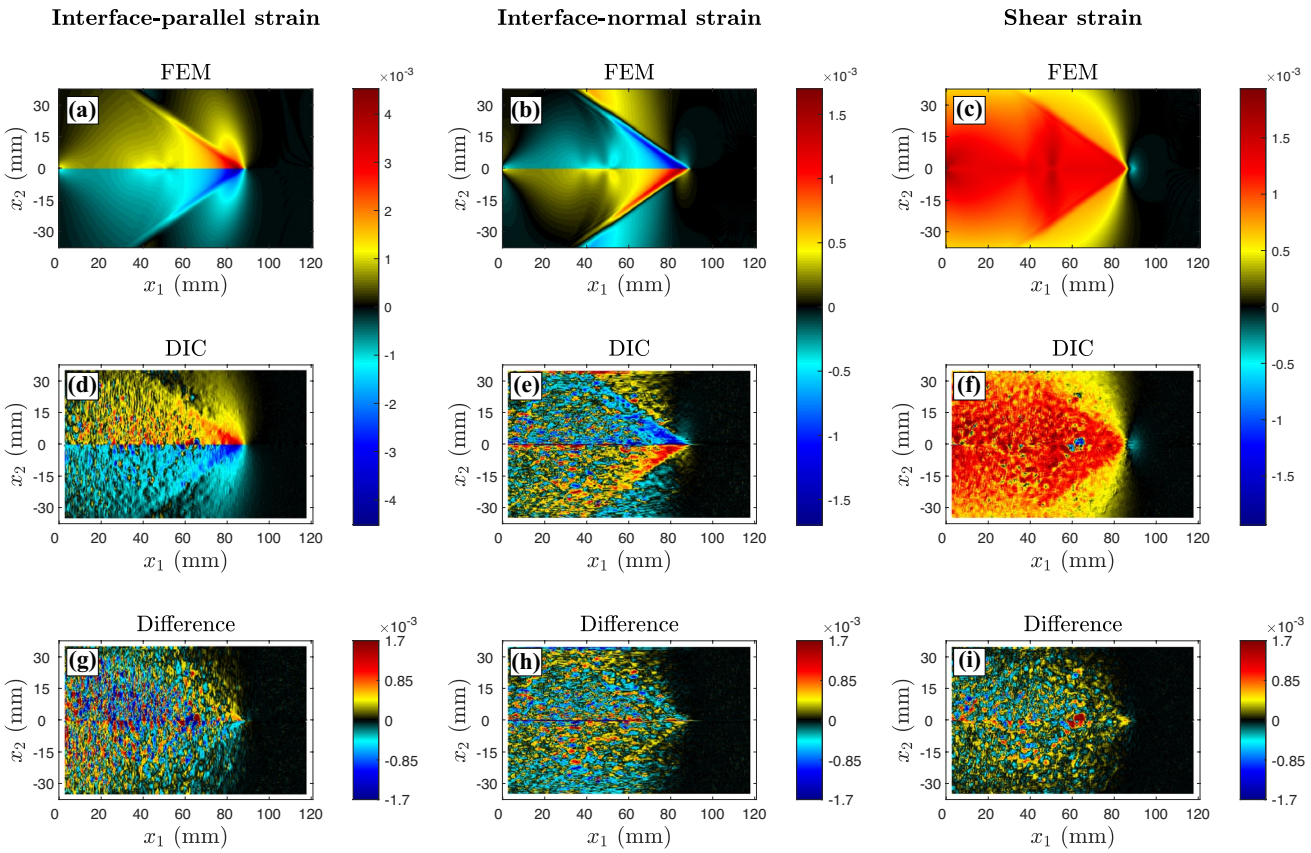

Fig. 17 Full-field strain components from the large FOV at $t = 45.9$ μs. Full-field maps obtained from the (**a**, **b**, **c**) FEM simulations and (**d**, **e**, **f**) DIC analysis. The DIC measurements are performed by employing a subset size of 11×11 pixel^2. (**g**, **h**, **i**) Evaluation of the DIC error through the difference between the FEM and DIC data

interface-parallel strain is well resolved, with a maximum (absolute) error of 0.0006 ε along the interface (Fig. 19(g)). In fact, the smoothing associated with a larger subset size has a positive effect on the strain computation, enhancing the quality of the signal without losing important features on the strain field, as shown by the path plots in Fig. 20(a, b).

The interface-normal strain structure is also well described by the DIC measurements (Fig. 19(b–e)), with the detection of the fine strain localization reaching ≈ 0.0017 ε (in absolute value). Nevertheless, an attenuation of this feature around 0.0002 ε is observed at the rupture tip, blunting the shear rupture front close to the interface (Fig. 19(h)). Moreover, the DIC strain field from the small FOV displays two horizontal anomalies equally distant from the specimen external borders, which can be ascribed to the data extrapolation performed by the "fill-boundary" algorithm half-subset away from the borders of the analysis domain. On the interface, the strain computation on extrapolated displacement data reproduces the trend from the FEM simulation, but all subsets grossly overestimate the reference FEM data, with the 41×41 pixel^2 subset minimizing such gap (Fig. 20(c)). This discrepancy is also observed in the ε_{22} vs. x_2 plot where the 41×41 pixel^2 subset overestimates the strain value on the interface, while reproducing the rest of the curve in good agreement with the reference FEM simulation data (Fig. 20(d)).

The increased spatial resolution provided by a the small FOV allows to distinguish the fine gradients characterizing the shear strain field ε_{12}, Fig. 19(c–f), with a maximum error of 0.0003 ε located in the crack tip region Fig. 19(i). The shear strain vs. position plots confirm that the 41×41 pixel^2 subset gives the best performances, since it reduces the noise and offers a reliable reproduction of the shear strain signal (Fig. 20(e, f)), except for a localized peak at $x_1 = 10.6$ mm, where the error is around 30% (Fig. 20(e)), and some outliers corresponding at the boundary between the main correlation and the "fill-boundary" domains (Fig. 20(f)).

Similarly to the particle velocity field, a cohesive length-to-subset size index $\lambda^*_{SB} > 1.5$ seems to ensure the inclusion

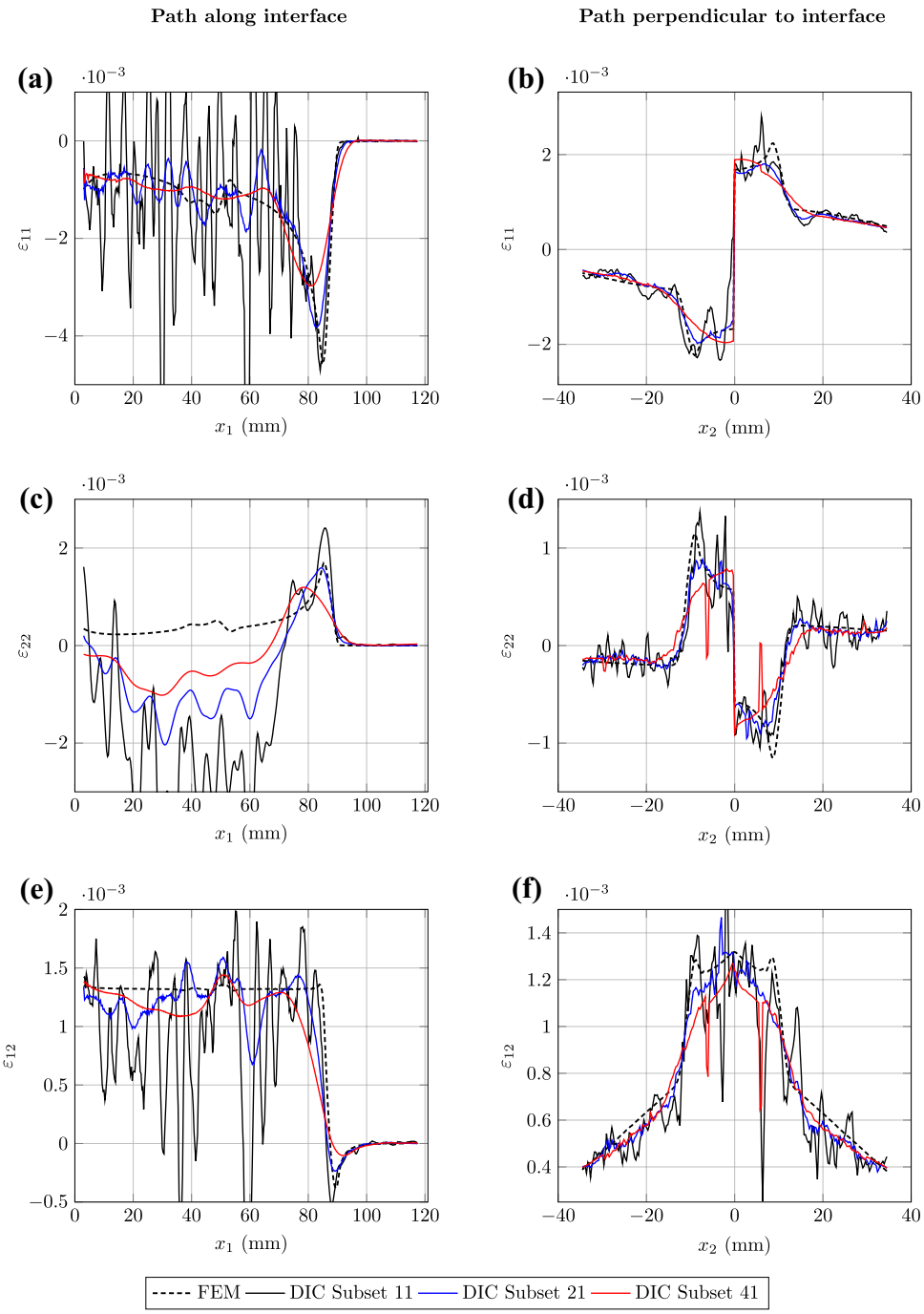

Fig. 18 Strain components vs. position along (**a**, **c**, **e**) and perpendicular (**b**, **d**, **f**) to the interface at $t = 45.9\ \mu$s for the large FOV. The plots compare the FEM simulations with the DIC measurements for different subset sizes

of all the the characteristic features of the strain structures in the two fields of view; this suggests the use of small subset for the large FOV, leading to a strong increase in the noise level. In turn, the noise mitigation requires the use of a bigger subset (i.e. 41×41 pixel^2) or to employ a wider virtual strain gauge (VSG)[1].

[1] According to [64], the VSG indicates the local region of the image (in pixel) involved in the calculation of the strain values at a specific location

Effect of the Order of Subset Transformation Functions

While the subset size is a primary analysis parameter for achieving an accurate measurement of the deformation field, a successful correlation also relies on the choice of the subset shape function. The subset shape functions describe the transformation of the subset due to the specimen deformation by employing polynomial functions [5, 68, 69]. Generally, the correlation algorithm inversely identifies these

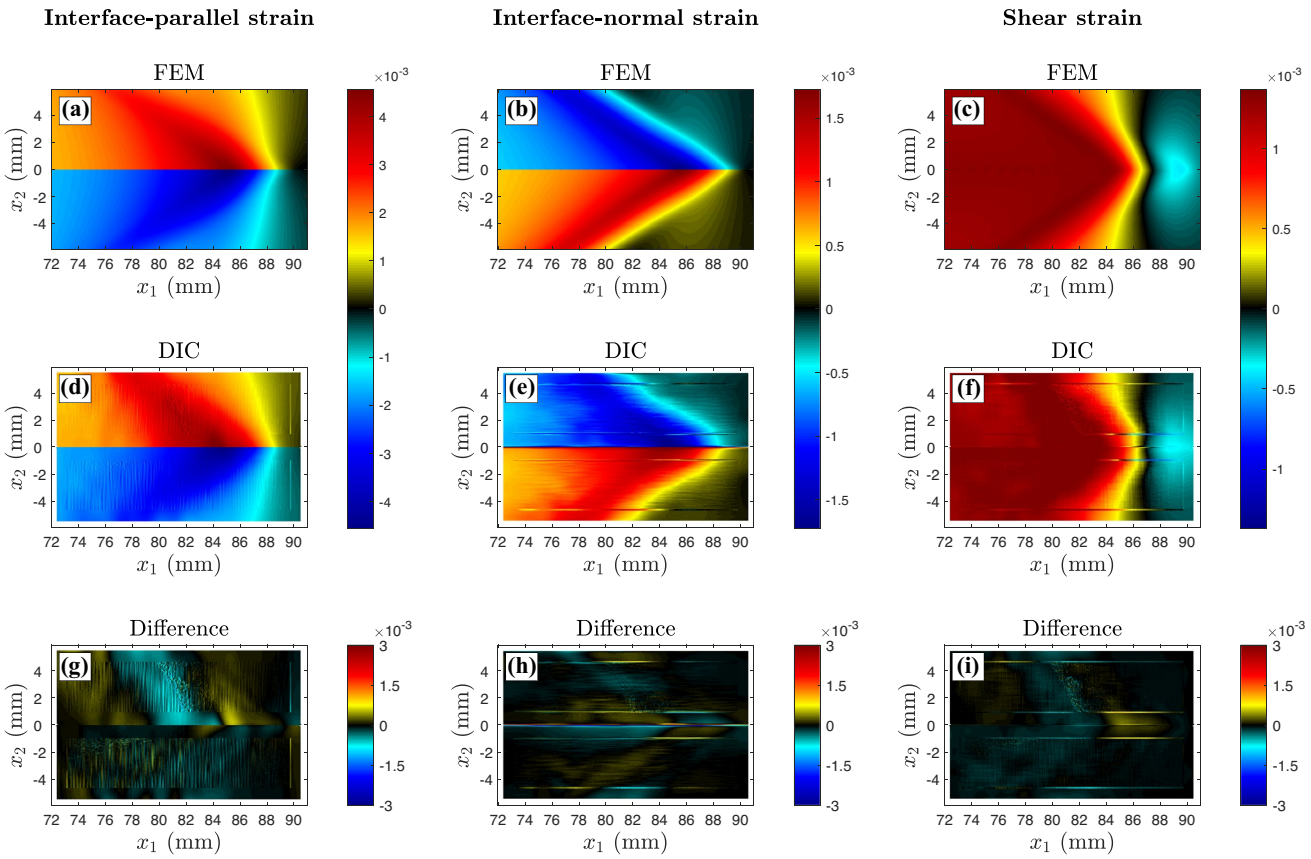

Fig. 19 Full-field strain components from the small FOV at $t = 45.9\ \mu$s. Full-field maps obtained from the (**a**, **b**, **c**) FEM simulations and (**d**, **e**, **f**) DIC analysis. The DIC measurements are performed by employing a subset size of 41×41 pixel^2. (**g**, **h**, **i**) Evaluation of the DIC error through the difference between the FEM and DIC data

parameters through the optimization of a correlation function (or criterion), which evaluates the similarity of the gray level distribution within each subset in the reference image and the deformed image. Since the DIC measures the average displacement of the subset – acting also like a filtering box – higher-order transformation functions allow to resolve a wider range of heterogeneous deformations, enhancing the subset matching, especially for larger subset sizes [69]. In the previous sections, we have quantified the DIC measurement error associated with the use of first-order polynomial functions, which describe affine transformations of the subset. In this section, we investigate the effects of the order of the polynomial functions. Specifically, we use the virtual experiment framework to the analyze the effect of second-order (quadratic) transformation functions.

The analysis presented so far is performed with the DIC software VIC-2D® 6. However, VIC-2D does not offer the possibility to select subset shape functions higher then first-order functions. In order to consider higher-order functions, we employ another commercial software, MatchID® (version 2020.1.1), keeping the same DIC settings reported in Table 2. Note that MatchID® allows the extrapolation of the correlation data up to the domain boundaries, using the same shape functions of the subsets closer to the edges to extrapolate the displacement fields [35]. To study the effect of the shape-function order, we compare the affine and quadratic shape functions in measuring the complex velocity and strain fields for the large FOV, employing two different subset sizes, 11×11 pixel^2 and 41×41 pixel^2. For consistency, we use the MatchID® software for all correlations discussed in this section.

The particle-velocity maps obtained using both linear and quadratic shape functions and the two subset sizes are shown in Fig. 21. The quadratic formulation with the 11×11 pixel^2 subset does not improve the reproduction of the sharp features of the interface-parallel particle velocity field compared to the affine counterpart (Fig. 21(c–e)), as also displayed by plots along paths parallel and perpendicular to the interface Fig. 22(a–c). The effect of the higher-order function is clearly observable with the 41×41 pixel^2 subset, allowing to include more details in proximity to the shear Mach cone. Nonetheless, the map still does not provide an exhaustive description of the field structure, indicating that the filtering imposed by the larger subset size has a predominant effect on the measured features.

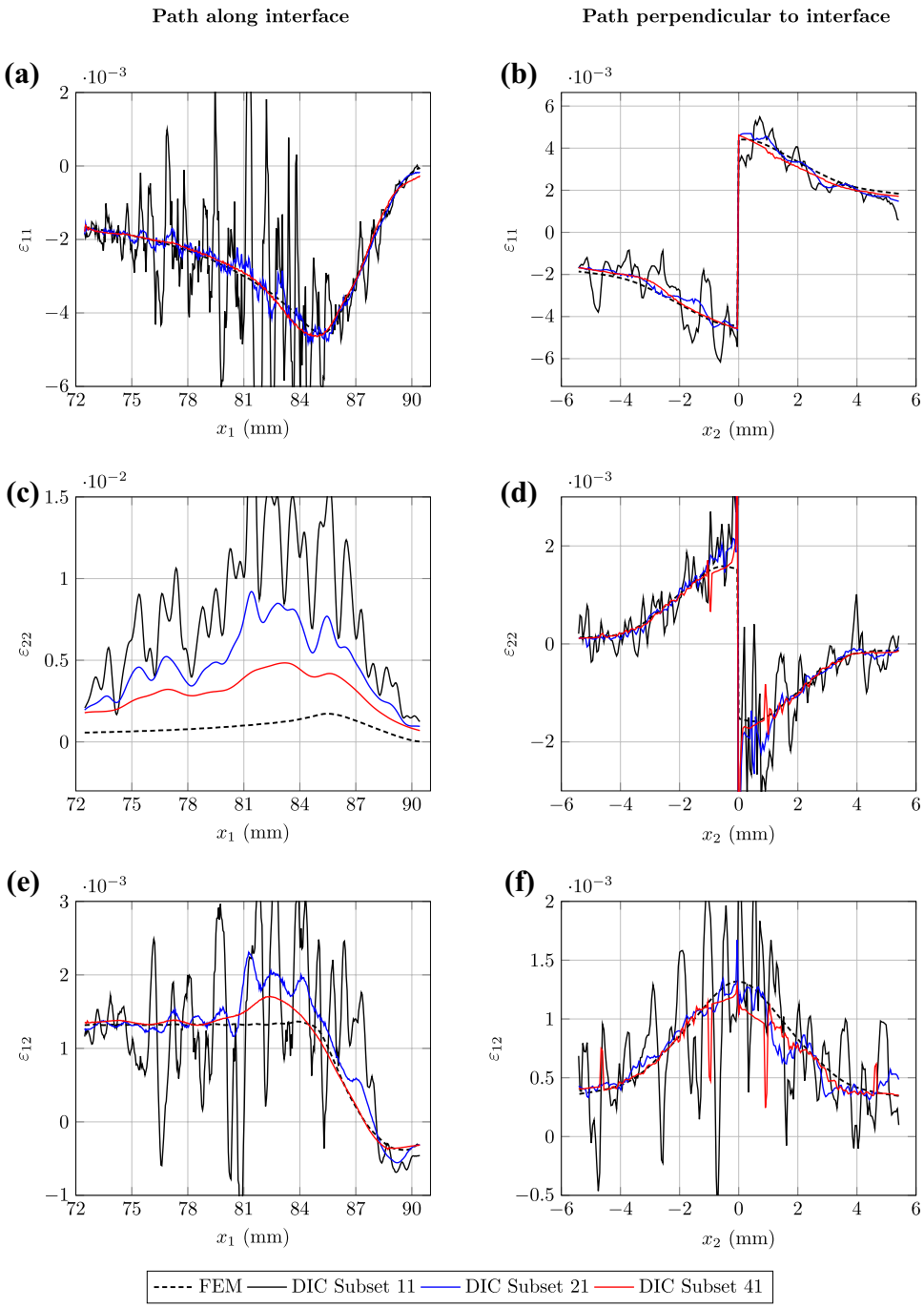

Fig. 20 Strain components vs. position along (**a**, **c**, **e**) and perpendicular (**b**, **d**, **f**) to the interface at $t = 45.9\ \mu$s for the small FOV. The plots compare the FEM simulations with the DIC measurements for different subset sizes

In contrast, the quadratic shape function with the 11×11 pixel^2 subset does enrich the description of the sharp features in the interface-normal particle velocity map, where the two positive wedge zones along the supershear fronts are well detected (Figs. 21(f) and 22(d)). However, the velocity fields obtained using the quadratic shape functions also result in a noisier behavior, when coupled with the 11×11 pixel^2 subset (e.g. Fig. 22(b)). This is likely because a smaller subset may not include a sufficient amount of information to identify the larger number of parameters in the ill-imposed correlation problem [69], degrading the quality of the full-field measurement. The DIC measurements obtained using the 41×41 pixel^2 subset, while capturing the main structure of the interface-normal velocity field with more details compared to the affine subset, do include a significant attenuation even by adopting the quadratic transformation functions (Fig. 21(h–j)).

Similar effects are observed analysing the full-field strain components, as shown in Fig. 23. In general, combining a small subset size with higher order transformation functions

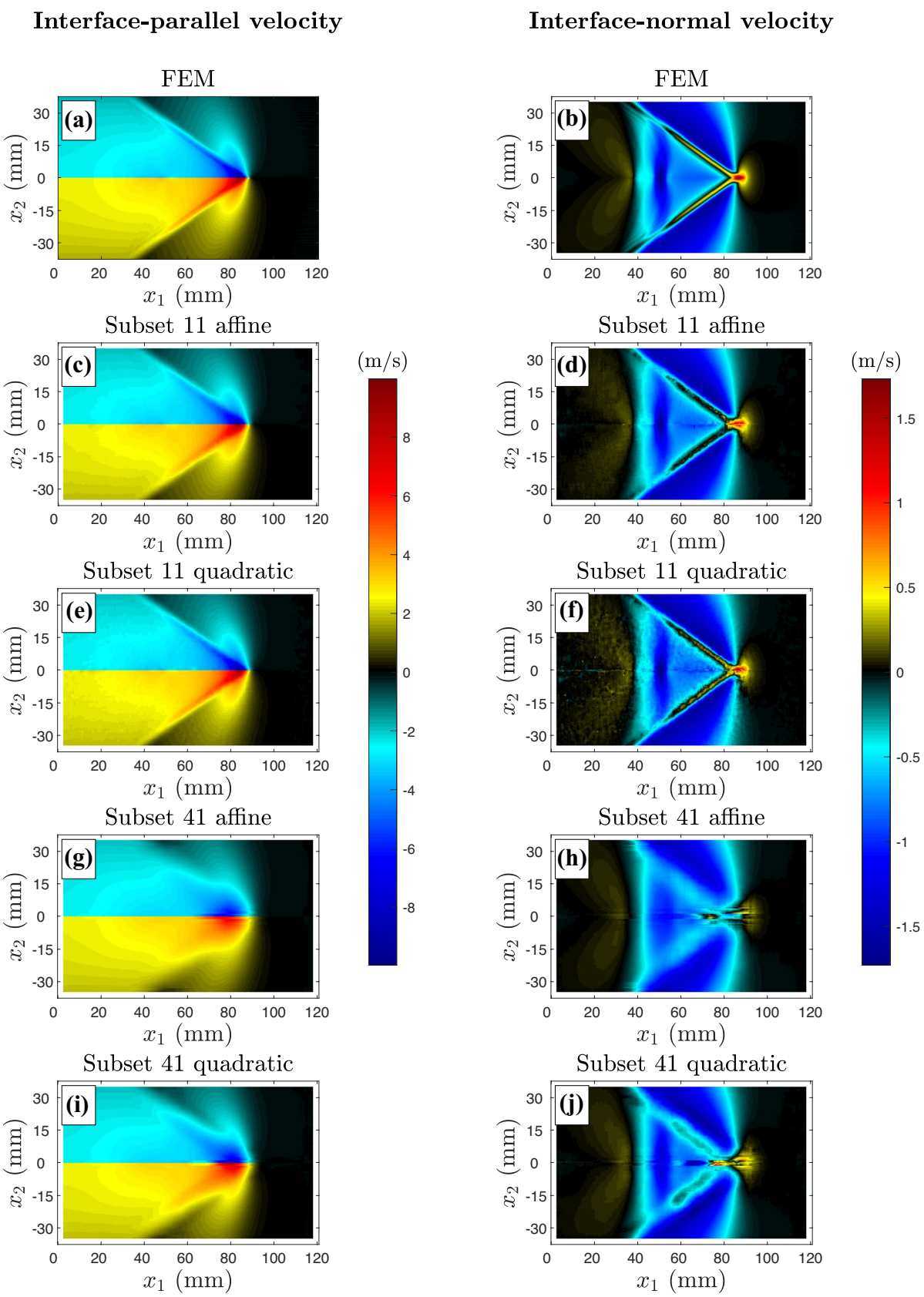

Fig. 21 Full-field particle velocity components from the large FOV at $t = 45.9\ \mu$s employing affine and quadratic transformation functions combined with 11×11 pixel^2 and 41×41 pixel^2 subsets

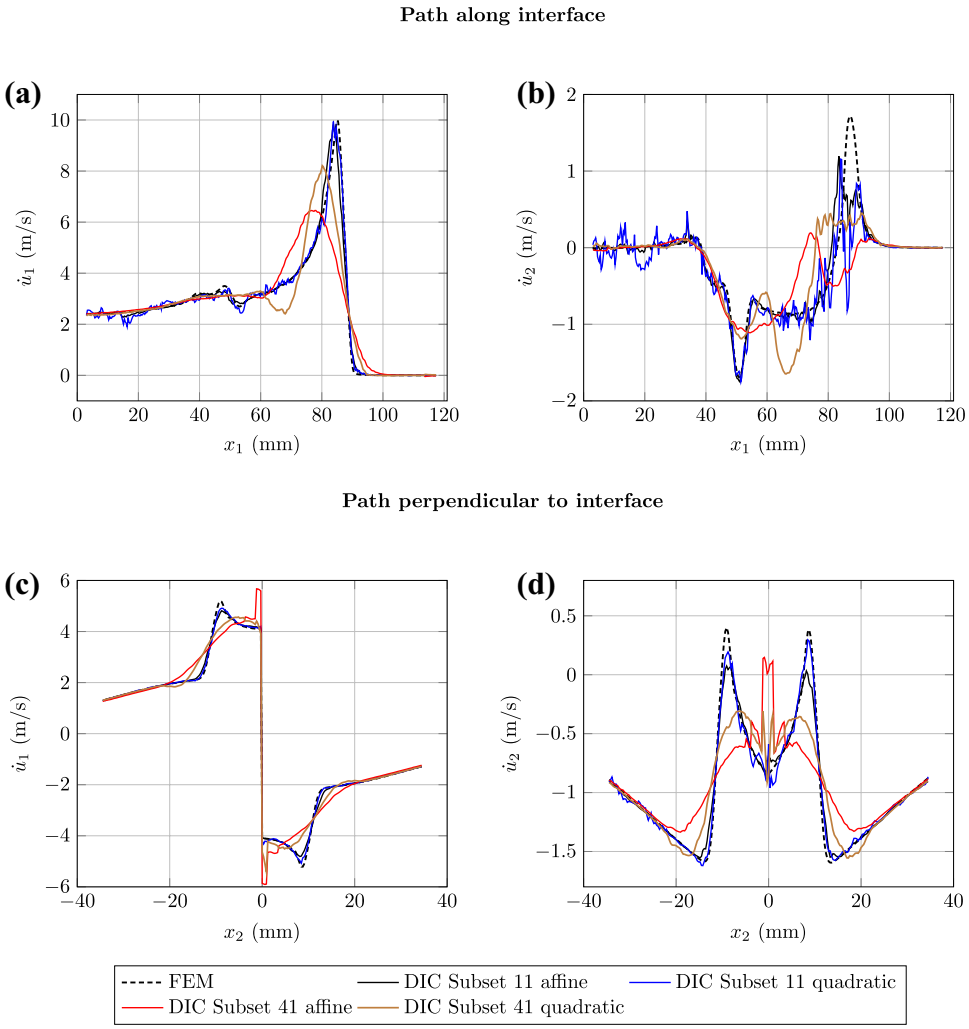

Fig. 22 Particle velocity components vs. position along the interface at $t = 45.9\ \mu$s for the large FOV. The charts compare the FEM analysis with DIC results employing affine and quadratic transformation functions combined with 11×11 pixel^2 and 41×41 pixel^2 subsets. All data has been sampled considering position paths along (**a**, **b**) and perpendicular (**c**, **d**) to the interface

improves the description of the sharp gradients, but the higher noise level does not produce an overall refinement of the field structures. This is particularly evident when plotting the strain components along path parallel and perpendicular to the interface (Fig. 24). On the other hand, the affine transformation functions with the 11×11 pixel^2 subset offers a clearer representation of the full-field features. As for the particle-velocity fields, quadratic shape functions improve the analysis outcomes when combined with 41×41 pixel^2 subset, but the averaging effect related to a larger subset size softens the sharp attributes characterizing the structures of the strain components.

Regardless of the noisy fluctuations of the signal, the measured strain components along the interface seem not to be influenced by the polynomial order used to describe the subset transformation, but mainly by the subset dimensions due to the characteristic length-scale of the phenomenon. The analysis on the data sampled along a vertical path at $x_1 = 72.6$ mm shows that the curves obtained through quadratic shape functions get qualitatively closer to the ground-truth signal from the FEM simulation, consistent with the observations in Fig. 23.

Reconstructing the Friction Behaviour From DIC Measurements

While the main purpose of this paper is to quantify the uncertainties associated with the full-field measurements of supershear ruptures, we introduce in this section a preliminary investigation on the derivation of the dynamic friction from our DIC analyses. The frictional behaviour at the interface is, in fact, a fundamental aspect governing the rupture propagation, and determining it has been the important application of the experimental DIC analysis. As reported in [24, 70], the experimental setup illustrated in "Laboratory Experiments Capturing Dynamic Shear Ruptures Using Ultrahigh-speed DIC" section has been employed to infer the complex evolution of friction associated with spontaneous propagating supershear cracks at different loading

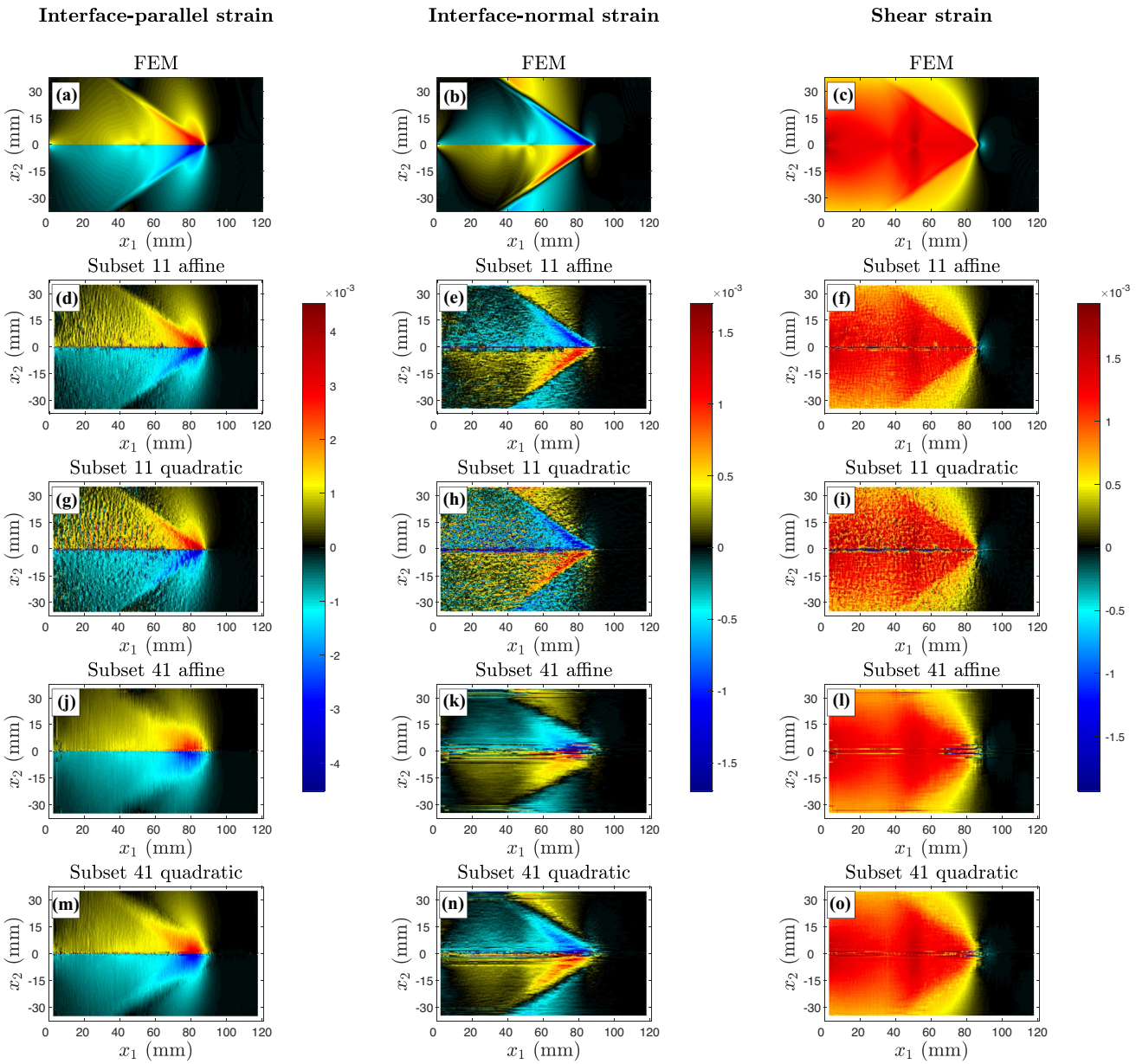

Fig. 23 Full-field strain components from the large field of view at $t = 45.9\ \mu$s measured by employing affine and quadratic transformation functions combined with the 11×11 pixel^2 and 41×41 pixel^2 subsets

conditions. The full-field measurement of displacements makes it possible to compute strains and, under bulk rheological assumptions, stresses, allowing to locally compute the friction coefficient at the interface, overcoming the main limitations of the traditional methods of friction estimation that rely on average measurements or measurements at a distance [71–74].

Here, we use the DIC maps to determine the evolution of friction on the interface, comparing it with the known slip-weakening friction assumed in the FEM simulation. The steps for the calculation of slip and friction coefficient from DIC measurements are the same as in [24]: slip is computed as the relative displacement across the interface from the maps of the two domains, while friction coefficient is obtained from the shear and normal stress fields. The stress fields are reconstructed from the strain fields displayed in "Full-field Strain Uncertainties" section using the constitutive equations of linear elasticity under the assumption of plane-stress conditions. The material coefficients are the same as in the FEM simulation. Since the DIC analysis takes as reference configuration the specimen under the quasi-static loading, the total stresses are retrieved by adding

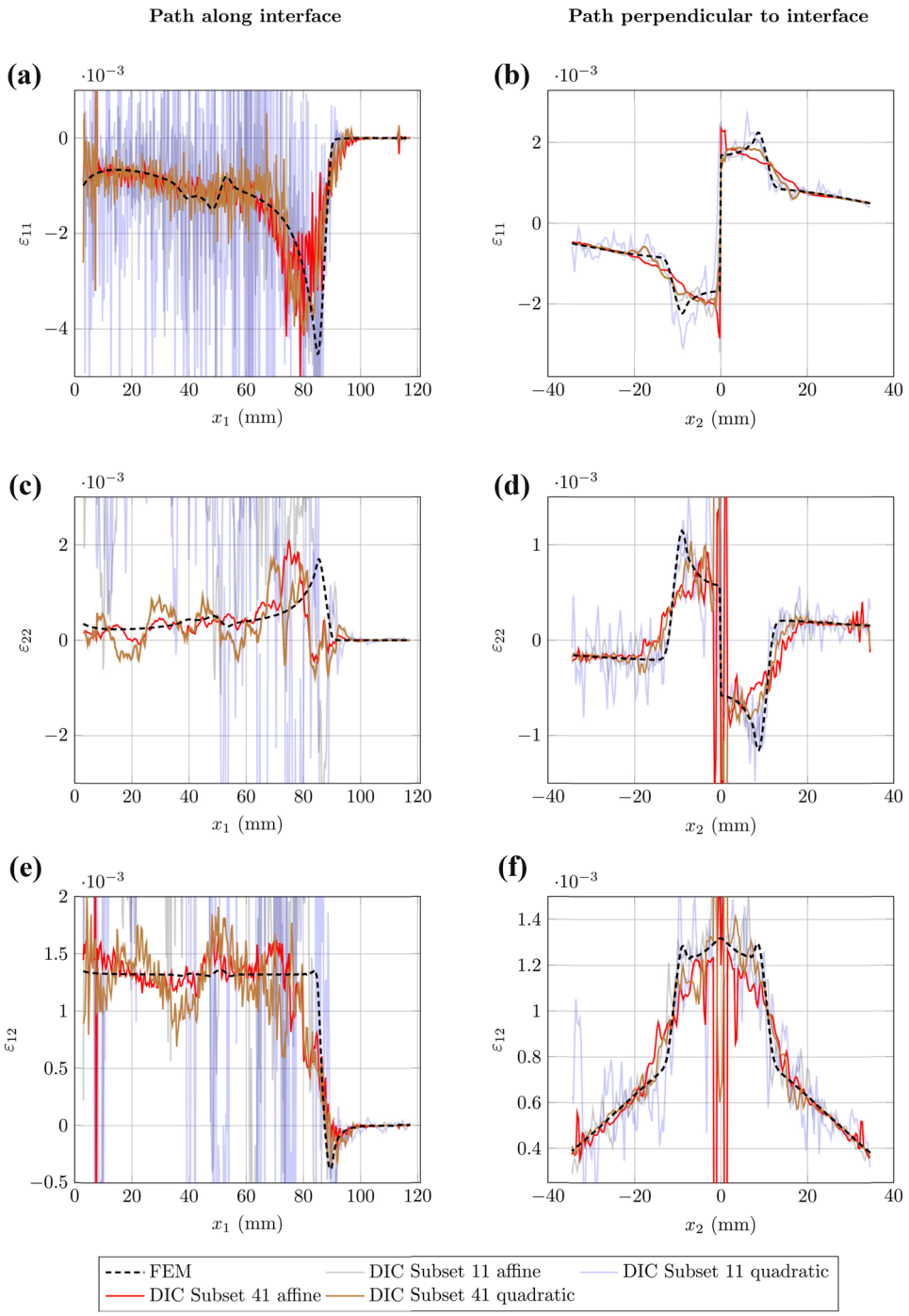

Fig. 24 Strain components vs. position along the interface at $t = 45.9\ \mu$s for the large field of view. The charts compare the FEM analysis with DIC results employing affine and quadratic transformation functions combined with 11×11 pixel^2 and 41×41 pixel^2 subsets. All data has been sampled considering position paths along (**a**, **c**, **e**) and perpendicular (**b**, **d**, **f**) to the interface

the stress components produced by the far-field load in the reference configuration to the DIC-measured stress changes.

In this preliminary analysis, there are some dissimilarities with the data processing for the friction analysis presented in [24]. As previously mentioned, since the correlation is performed on pure synthetic images, we do not impose the "symmetry-adjustment" procedure described in [25] to enforce symmetry/anti-symmetry to the interface-normal and interface-parallel displacement components. In addition, we do not apply either the averaging procedure on the slip and friction curves among contiguous measurement points or the "traction continuity" procedure described at the interface as in [27, 28]. Investigating the effect of those procedures in the presence of different sources of experimental noise will be the focus of future work. We do use in this initial evaluation filtered DIC displacement data by employing a non-local means (NL-Means) scheme [75, 76]. For the filtering process, we adopt the same settings as in previous experimental works [24, 25].

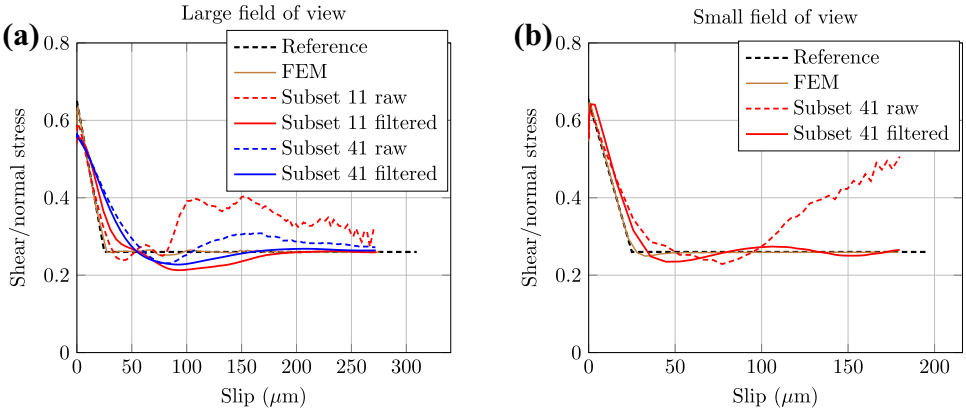

Fig. 25 Inferred friction vs. slip behaviour from the DIC measurements compared with the assumed friction. The experimental study of dynamic friction by [24] used the small FOV with the 41×41 pixel^2 subset, as in panel (**b**)

Let us consider the DIC-inferred friction evolution for a single measurement point at the middle of the FOV for both the large and small FOV (Fig. 25). For the small FOV with the 41×41 pixel^2 subset, which is the one used in the experimental study of [24] to study dynamic friction, the friction evolution is reproduced quite well for the filtered data, including the peak (static) friction coefficient, although the weakening slope is somewhat milder, resulting in about 25% larger slip weakening distance. For the large FOV (Fig. 25(a)), the 11×11 pixel^2 subset also does a reasonable job, although the static friction coefficient f_s is underestimated (known value 0.65, inferred value 0.59) and the linear slop is also milder than the actual one. The inferred f_d presents values close to the constant reference value but oscillating around it, attributable to the errors in inferring interface-normal strain. Increasing the subset size to 41×41 pixel^2 helps to average out such oscillations; however, the filtering effect associated with the larger subset reduces both the inferred peak friction and the slope of the weakening phase. For both subset sizes, the NL-Means filter smoothes the measured dynamic friction coefficient but at the cost of losing the accuracy in resolving the linear-weakening phase of the curve.

Note that the large FOV would represents a challenging configuration for measuring the static friction coefficient, since the 11×11 pixel^2 subset would result in additional sources of noise not considered here and the 41×41 pixel^2 subset significantly modifies the inferred evolution, decreasing the peak friction and almost doubling the slip-weakening distance. In contrast, the small FOV with the 41×41 pixel^2 subset reproduces the initial part of the friction curve quite well (Fig. 25(b)). When the slip reach 100 μm, however, the unfiltered friction signal increases due to presence of outliers along the interface in the interface-normal stress map[2]. The application of the NL-Means filter on the displacement data is beneficial for the friction computation in this case, as it allows to produce a more regularized signal in the strain fields. Even though the friction vs. slip curve is retrieved from a single measurement point, without any averaging procedure among nearby points (to reduce noise) as done in experimental studies, the linear slip weakening law is reconstructed with high fidelity.

A correlation between the physical size of the subset and the accuracy persists in measuring the friction vs. slip curves: subsets characterized by similar physical dimensions – and, in turn, similar λ^*_{SB} ratios – provide similar results for the identification of the weakening phase (see the raw curves for subsets 11×11 pixel^2 in the large FOV and 41×41 pixel^2 in the small FOV). The small FOV with the 41×41 pixel^2 does a better job since it has a better λ^*_{SB} ratio as well as a benefit of correlating over a larger subset, which would have additional importance in the laboratory experiments with have additional sources of noise, as discussed in the next section.

Conclusions

Understanding the impact of the uncertainties associated with ultrahigh-speed digital image correlation is a key issue to accurately quantify the the full-field evolution of complex phenomena such as dynamic ruptures. In this study, we have introduced a virtual experiment framework in order to numerically reproduce the laboratory earthquake experiments featuring dynamic ruptures and test the accuracy of the measurements. Speckled images are synthetically deformed using finite element simulations and are subsequently analyzed with digital image correlation algorithms like in a laboratory experiment. The error is quantified by comparing the DIC maps with the ground-truth FEM simulations, over two fields of view (FOV) of different sizes.

The following general conclusion can be drawn:

- Resolving sharp features at the rupture tip: Sharp evolving features at the rupture tip scale with the cohesive zone length, that is, the size of the region behind the rupture tip where the shear stress evolves from its peak

[2] These outliers can be also observed from the interface-normal strain and are highlighted in Fig. 19(h).

value to its dynamic value. If the physical dimension of the DIC subset size resolves the cohesive zone length at least by a factor of 1.5 or better ($\lambda^*_{SB} > 1.5$), there is adequate to excellent recovery of various associated features, such as positive interface-normal motion at the rupture tip and peak slip rates and their location. This holds for all the subsets considered here for the small FOV, and for the smallest, 11×11 pixel^2, subset for the large FOV. Larger subsets for the large FOV increasingly over-average the fields, resulting in progressive loss of features, decreased peaks, and blunted shocks.

- Trade-off between feature resolution and reducing noise: Larger subset sizes, such as 41×41 pixel^2, allow for correlations over more speckle pattern features and introduce additional smoothing, helping reduce noise and affecting especially the derived quantities, such as particle velocities and strains. For the large FOV, this comes with the cost of over-averaging the physical aspects of the problem with larger subset sizes. For the small FOV, since all subsets resolve the physical scales of the problem, the larger subsets generally perform better, especially when derived quantities are to be computed.
- Effect of the subset transformation functions: The sharp features displayed by particle velocity fields are well-resolved with the affine (linear) transformation functions if the subset size is small enough to resolve the cohesive zone length. In general, increasing the order of the polynomial transformation functions associated with the subset allows to enhance the observation of finer details, such as for example the positive wedge in interface-normal velocity along the shock fronts.
- Friction measurements: As preliminary evaluation of the uncertainties associated with friction measurements using ultrahigh-speed DIC, the magnified resolution of the rupture tip by the small FOV offers a close identification of the friction law. The analysis reveals that the DIC measurement is capable of resolving properly the friction evolution, even though there is no direct measurement at the interface and the field is reconstructed by means of interpolation by the "fill-boundary" algorithm. Nevertheless, the friction calculation is strongly affected by the noise in the strain signal, which requires the application of a filtering procedure to get accurate results. The reduced spatial resolution of the large FOV significantly reduces the accuracy of the friction inference.
- Selection of the FOV and subset size: faced with the fixed and limited pixel sizes of the high-speed cameras and these conclusions, one has to make difficult choices regarding the FOV and subset size. To resolve sharp features at the rupture front with minimal noise, one needs relatively large subsets of 41×41 pixel^2 which also need to be less than half of the cohesive zone length in the physical dimension. Given the pixel sizes of camera images (400×250 in the experimental studies by Rubino et al. [24, 25]), this implies that the FOV cannot be much more than 5 by 3 cohesive zone lengths, dramatically limiting the size of the imaged area. A much larger FOV comes at the expense of either noise for a small subset size (such as the large FOV in this study with 11×11 pixel^2 subset), or blurring spatial features due to a large subset size that does not resolve the cohesive zone (such as the large FOV here with 41×41 pixel^2 subset). Perhaps an optimal approach to experimental design would be to repeat experiments with different FOVs, starting with a small FOV that would enable capturing the cohesive zone and identifying its size, and then using larger FOV with appropriately selected subset sizes that still resolve the cohesive zone, at least marginally.

Note that while this analysis based on the virtual experiment is crucial to identify the effect of the subset size and transformation-function order on reconstructing the source signal, further modeling is needed to fully understand the DIC analysis of the experimental ruptures. For example, the presented analysis indicates that the large FOV with the subset size of 41×41 pixel^2 is not capable of capturing the shock features in the particle velocity fields. However, the velocity fields obtained in a real experiment, performed under the same loading, and using the same large FOV and subset size of 41×41 pixel^2, do exhibit shock features, particularly in the interface-parallel component [25]. This is likely due to the fact that the shock fronts exhibited by the numerical ruptures are sharper than those in the experimental ruptures. In fact, in the virtual experiment, the particle velocity has a rapid drop behind the rupture tip (from a peak of 10 m/s at the rupture tip to 2m/s behind) and the shock fronts are very localized features, whereas the experimental profiles obtained using both DIC and laser velocimeters show a milder change (from 10 m/s to 4 m/s).

The difference between the simulated and experimental ruptures is, in turn, likely due to the simplified modeling assumptions, including an approximation to the initiation procedure and the 2-D nature of the simulation vs. 3-D nature of the experiment. Another simplifying modeling assumption is the form of the friction law, with the modeling employing linear slip-weakening friction while the experimental friction exhibiting rate-and-state effects with flash heating; while the two friction types can be chosen to have similar variations of shear stress with slip at some points on the interface, the effective slip-weakening relation is likely to vary some along the interface in the actual experiment, especially during rupture initiation and acceleration. Yet another simplifying assumption in the numerical simulations is linear elastic behavior, whereas the materials used in the experiments are viscoelastic. The viscoelastic nature of the polymers used in the experiments may widen the Mach cone features. It also leads to the development of another set of Mach features [29], due to the dilatational field. These additional sharp features, observed experimentally, are not present in the

numerical simulations based on linear elastic constitutive laws. Further simulations exploring a wider range of modeling parameters and constitutive laws would help address their effects on the rupture behavior and provide DIC parameters more directly applicable to the analysis of laboratory experiments.

Future developments of the presented virtual experiment framework will also aim to quantify other sources of measurement uncertainty, including high-speed camera noise, environmental factors (such as lighting variations during the acquisition of the image sequence), and the type and size of the speckle pattern. The assessment of these error sources would help maximize the performances of the ultrahigh-speed DIC measurements, and explore the impacts of post-processing filters and the effects of the virtual strain gauge size on the strain computation. In addition, further studies need to investigate the capability of DIC measurements to capture the evolution of more complex friction behaviors during spontaneous rupture propagation, evaluating the accuracy in deriving frictional parameters.

Appendix 1

Friction Description and Rupture Nucleation in the Numerical Simulations

The numerical model adopted the linear slip-weakening formulation for the description of friction evolution [65]. In this formulation, the friction coefficient is given by:

$$f = \begin{cases} f_s - (f_s - f_d)\dfrac{\delta}{D_c}\,, & \delta \le D_c \\ f_d\,, & \delta > D_c \end{cases} \tag{1}$$

where f_s and f_d are the static and dynamic friction coefficients and D_c is the critical slip distance over which f_d is reached. We employ $f_s = 0.65$, $f_d = 0.26$, and $D_c = 25\,\mu$m obtained experimentally [24] under the same loading conditions as used in the simulations.

Dynamic rupture nucleation is obtained by artificially modifying the frictional properties in a small region around the desired nucleation size (Fig. 1(c)). In the nucleation region, the frictional behavior is described by the linear slip-weakening law given by equation (1), with modified parameters ($f_s^* = 0.22$, $f_d^* = 0.01$, $D_c^* = 0.05\,\mu$m) obtained through an iterative process in order to produce a rupture propagation consistent with the actual experiment. At the beginning of the simulation, the lower frictional strength over the nucleation region compared to the applied pre-stress level result in the initiation of a dynamic rupture. Note that this procedure is similar to reducing the normal stress due to wire explosion with the higher friction coefficients.

The length of the nucleation region $2L^*$ can be obtained from the critical nucleation length $2L_c$, which indicates the minimum size of the initial slip region required to induce a dynamic instability. The half-length L_c is computed as [55, 77]:

$$L_c = \frac{\mu}{\pi(1-\nu)}\,\frac{(f_s - f_d)D_C}{P(\sin\alpha - f_d\cos\alpha)^2}\,, \tag{2}$$

where $\mu = E/[2(1+\nu)]$ is the shear modulus and ν is the Poisson coefficient. The nucleation length was taken 1.2 times L_c, so that $2L^* = 14.76$ mm.

Another relevant quantity that characterizes the spatial resolution of the dynamic crack is the cohesive zone length Λ_0, which indicates the portion of the interface, behind the fracture tip, where the static shear stress transitions to its dynamic value [55, 65, 78]. For a Mode II crack, the cohesive zone length of a crack advancing with a near-zero rupture speed can be estimated as follows:

$$\Lambda^0 = \frac{9\pi}{32(1-\nu)}\,\frac{\mu D_c}{(f_s - f_d)P\cos^2\alpha}\,. \tag{3}$$

Note that this formula describes the cohesive zone associated with a quasi-static rupture, while the cohesive length for dynamic rupture is generally smaller [1, 66]. According to equation (3), the estimated cohesive zone length is $\Lambda^0 = 9.72$ mm.

Appendix 2

Computation of the Velocity and Strain Fields

The particle-velocity maps are obtained from the displacement fields using a central difference scheme for the time differentiation, i.e:

$$\dot{u}_1(x_1, x_2, t) = \frac{u_1(x_1, x_2, t+1) - u1(x_1, x_2, t-1)}{\Delta t}\,, \tag{4}$$

$$\dot{u}_2(x_1, x_2, t) = \frac{u_2(x_1, x_2, t+1) - u2(x_1, x_2, t-1)}{\Delta t}\,, \tag{5}$$

Similarly, the strain fields are obtained at each timestep t, for data points away from the boundaries, using a central difference algorithm:

$$\varepsilon_{11}(x_1, x_2) = \frac{u_1(x_1, x_2 + p) - u_1(x_1, x_2 - p)}{2p}\,, \tag{6}$$

$$\varepsilon_{22}(x_1, x_2) = -\frac{u_2(x_1 + p, x_2) - u_2(x_1 - p, x_2)}{2p}\,, \tag{7}$$

$$\varepsilon_{12}(x_1, x_2) = \frac{1}{2}\left[-\frac{u_1(x_1 + p, x_2) - u_1(x_1 - p, x_2)}{2p} + \frac{u_2(x_1, x_2 + p) - u_2(x_1, x_2 - p)}{2p}\right], \tag{8}$$

where p indicates the pitch distance between two measurement points. Here we choose $p = 1$ according to the stepsize of 1 pixel imposed in the DIC analysis. Close to the contact interface, the strain fields are derived using the backward and forward difference scheme for data points above and below the interface, respectively. For instance, according to the forward finite difference scheme, the strain components are computed through three points as:

$$\varepsilon_{11}(x_1, x_2) = \frac{-u_1(x_1, x_2 + 2p) + 4u_1(x_1, x_2 + p) - 3u_1(x_1, x_2)}{2p}, \tag{9}$$

$$\varepsilon_{22}(x_1, x_2) = \frac{-u_2(x_1 + 2p, x_2) + 4u_2(x_1 + p, x_2) - 3u_2(x_1, x_2)}{2p}, \tag{10}$$

$$\varepsilon_{12}(x_1, x_2) = \frac{1}{2}\left[-\frac{-u_1(x_1 + 2p, x_2) + 4u_1(x_1 + p, x_2) - 3u_1(x_1, x_2)}{2p} + \frac{-u_2(x_1, x_2 + 2p) + 4u_2(x_1, x_2 + p) - 3u_2(x_1, x_2)}{2p}\right]. \tag{11}$$

Acknowledgements V.R. and A.J.R. would like to acknowledge the support of NSF (Grant EAR-1651235 and EAR-1651235), the US Geological Survey (USGS) (Grant G20AP00037), the NSF-IUCRC at California Institute of Technology-Center for Geomechanics and Mitigation of Geohazards (GMG), and the Southern California Earthquake Center (SCEC). SCEC is funded by NSF Cooperative Agreement EAR-1033462 and USGS Cooperative Agreement G12AC20038. V.R. thanks Fabrice Pierron for insightful discussions on the uncertainty quantification of DIC measurements.

Author Contributions Conceptualization: Attilio Lattanzi, Vito Rubino, Marco Rossi, Ares J. Rosakis, Nadia Lapusta; Methodology: Attilio Lattanzi, Vito Rubino, Marco Rossi; Formal analysis: Attilio Lattanzi, Alex Donzelli; Investigation: Attilio Lattanzi; Software: Attilio Lattanzi, Vito Rubino, Marco Rossi; Visualization: Attilio Lattanzi; Writing – original draft: Attilio Lattanzi, Vito Rubino; Writing – review & editing: Marco Rossi, Ares J. Rosakis, Nadia Lapusta.

Data Availability The datasets generated and analysed during the current study are available from the corresponding author on reasonable request.

Declarations

Conflicts of Interest The authors have no competing interests to declare that are relevant to the content of this article.

References

1. Freund LB (1990) Dynamic fracture mechanics. Cambridge University Press. https://doi.org/10.1017/cbo9780511546761
2. Rice JR, Lapusta N, Ranjith K (2001) Rate and state dependent friction and the stability of sliding between elastically deformable solids. J Mech Phys Solids 49(9):1865–1898. https://doi.org/10.1016/s0022-5096(01)00042-4
3. Coker D, Rosakis AJ (2001) Experimental observations of intersonic crack growth in asymmetrically loaded unidirectional composite plates. Philos Mag A 81(3):571–595. https://doi.org/10.1080/01418610108212160
4. Scholz CH (2018) The mechanics of earthquakes and faulting. Cambridge University Press. https://doi.org/10.1017/9781316681473
5. Sutton MA, Orteu JJ, Schreier H (2009) Image correlation for shape. Springer, Motion and Deformation Measurements
6. Reu PL (2011) High/ultra-high speed imaging as a diagnostic tool. In: Advances in Experimental Mechanics VIII. Applied Mechanics and Materials, vol 70. Trans Tech Publications Ltd, pp 69–74. https://doi.org/10.4028/www.scientific.net/AMM70.69
7. Grédiac M, Hild F (2012) Full-field measurements and identification in solid mechanics. Wiley
8. Sutton MA, Matta F, Rizos D, Ghorbani R, Rajan S, Mollenhauer DH, Schreier HW, Lasprilla AO (2016) Recent progress in digital image correlation: background and developments since the 2013 W M Murray lecture. Exp Mech 57(1):1–30. https://doi.org/10.1007/s11340-016-0233-3
9. Weidner A, Biermann H (2021) Review on strain localization phenomena studied by high-resolution Digital Image Correlation. Adv Eng Mater 2001409
10. Silvani C, Réthoré J, Nicaise S (2021) Measuring coarse grain deformation by digital image correlation. Strain. https://doi.org/10.1111/str.12378
11. Pan Z, Huang S, Su Y, Qiao M, Zhang Q (2020) Strain field measurements over 3000 c using 3D-digital image correlation. Opt Lasers Eng 127:105942
12. Rossi M, Cortese L, Genovese K, Lattanzi A, Nalli F, Pierron F (2018) Evaluation of volume deformation from surface DIC measurements. Exp Mech 58:1181–1194. https://doi.org/10.1007/s11340-018-0409-0
13. Rossi M, Pierron F, Forquin P (2013) Assessment of the metrological performance of an *in situ* storage image sensor ultra-high speed camera for full-field deformation measurements. Meas Sci Technol 25(2):025401. https://doi.org/10.1088/0957-0233/25/2/025401
14. Pierron F, Zhu H, Siviour C (2014) Beyond Hopkinson's bar. Philos Trans R Soc A Math Phys Eng Sci 372(2023):20130195. https://doi.org/10.1098/rsta.2013.0195
15. Hild F, Bouterf A, Forquin P, Roux S (2017) On the use of digital image correlation for the analysis of the dynamic behavior of materials. In: The Micro-World Observed by Ultra High-Speed Cameras. Springer, pp 185–206. https://doi.org/10.1007/978-3-319-61491-5_8
16. Rosakis AJ, Rubino V, Lapusta N (2020) Recent milestones in unraveling the full-field structure of dynamic shear cracks and fault ruptures in real-time: from photoelasticity to ultrahigh-speed digital image correlation. J Appl Mech 87(3). https://doi.org/10.1115/1.4045715
17. Rubino V, Lapusta N, Rosakis AJ, Leprince S, Avouac JP (2015) Static laboratory earthquake measurements with the digital image correlation method. Exp Mech 55(1):77–94. https://doi.org/10.1007/s11340-014-9893-z
18. Siebert T (2007) High-speed digital image correlation: error estimations and applications. Opt Eng 46(5):051004. https://doi.org/10.1117/1.2741217
19. Kirugulige MS, Tippur HV, Denney TS (2007) Measurement of transient deformations using digital image correlation method and high-speed photography: application to dynamic fracture. Appl Opt 46(22):5083. https://doi.org/10.1364/ao.46.005083
20. Gao G, Huang S, Xia K, Li Z (2015) Application of digital image correlation (DIC) in dynamic notched semi-circular bend (NSCB) tests. Exp Mech 55(1):95–104. https://doi.org/10.1007/s11340-014-9863-5
21. Koohbor B, Kidane A, Sutton MA, Zhao X, Mallon S (2017) Analysis of dynamic bending test using ultra high speed DIC and the virtual fields method. Int J Impact Eng 110:299–310. https://doi.org/10.1016/j.ijimpeng.2016.12.021
22. Kojima T, Kimura Y, Arikawa S, Notomi M (2021) Evaluation of dynamic fracture toughness of a bonded bi-material interface subject to high-strain-rate shearing using digital image correlation. Eng Fract Mech 241:107391

23. Ravindran S, Shankar G, Suwas S, Narasimhan R et al (2021) Fracture mechanism and toughness of a rolled magnesium alloy under dynamic loading. Acta Mater 202:350–365
24. Rubino V, Rosakis AJ, Lapusta N (2017) Understanding dynamic friction through spontaneously evolving laboratory earthquakes. Nat Commun. https://doi.org/10.1038/ncomms15991
25. Rubino V, Rosakis AJ, Lapusta N (2019) Full-field ultrahigh-speed quantification of dynamic shear ruptures using Digital Image Correlation. Exp Mech 59:551–582
26. Rubino V, Rosakis AJ, Lapusta N (2020) Spatiotemporal properties of sub-Rayleigh and supershear ruptures inferred from full-field dynamic imaging of laboratory experiments. J Geophys Res Solid Earth 125(2). https://doi.org/10.1029/2019jb018922
27. Tal Rubino (2019) Rosakis, Lapusta: Enhanced digital image correlation analysis of ruptures with enforced traction continuity conditions across interfaces. Appl Sci 9(8):1625. https://doi.org/10.3390/app9081625
28. Tal Y, Rubino V, Rosakis AJ, Lapusta N (2020) Illuminating the physics of dynamic friction through laboratory earthquakes on thrust faults. Proc Natl Acad Sci 117(35):21095–21100. https://doi.org/10.1073/pnas.2004590117
29. Gori M, Rubino V, Rosakis AJ, Lapusta N (2018) Pressure shock fronts formed by ultra-fast shear cracks in viscoelastic materials. Nat Commun 9(1). https://doi.org/10.1038/s41467-018-07139-4
30. Kondo Y, Takubo K, Tominaga H, Hirose R, Tokuoka N, Kawaguchi Y, Takaie Y, Ozaki A, Nakaya S, Yano F, Daigen T (2013) Development of "hypervision hpv-x" high-speed video camera
31. Tochigi Y, Hanzawa K, Kato Y, Kuroda R, Mutoh H, Hirose R, Tominaga H, Takubo K, Kondo Y, Sugawa S (2013) A global-shutter CMOS image sensor with readout speed of 1-tpixel/s burst and 780-mpixel/s continuous. IEEE J Solid-State Circuits 48(1):329–338. https://doi.org/10.1109/jssc.2012.2219685
32. Lykotrafitis G, Rosakis AJ, Ravichandran G (2006) Self-healing pulse-like shear ruptures in the laboratory. Science 313(5794):1765–1768. https://doi.org/10.1126/science.1128359
33. Lava P, Cooreman S, Coppieters S, De Strycker M, Debruyne D (2009) Assessment of measuring errors in DIC using deformation fields generated by plastic FEA. Opt Lasers Eng 47(7):747–753. https://doi.org/10.1016/j.optlaseng.2009.03.007
34. Lava P, Cooreman S, Debruyne D (2010) Study of systematic errors in strain fields obtained via DIC using heterogeneous deformation generated by plastic FEA. Opt Lasers Eng 48(4):457–468. https://doi.org/10.1016/j.optlaseng.2009.08.013
35. Rossi M, Lava P, Pierron F, Debruyne D, Sasso M (2015) Effect of DIC spatial resolution, noise and interpolation error on identification results with the VFM. Strain 51:206–222
36. Badaloni M, Rossi M, Chiappini G, Lava P, Debruyne D (2015) Impact of experimental uncertainties on the identification of mechanical material properties using DIC. Exp Mech 55(8):1411–1426
37. Reu PL, Toussaint E, Jones E, Bruck HA, Iadicola M, Balcaen R, Turner DZ, Siebert T, Lava P, Simonsen M (2018) DIC challenge: developing images and guidelines for evaluating accuracy and resolution of 2D analyses. Exp Mech 58(7):1067–1099. https://doi.org/10.1007/s11340-017-0349-0
38. Jones EMC, Carroll JD, Karlson KN, Kramer SLB, Lehoucq RB, Reu PL, Turner DZ (2018) Parameter covariance and non-uniqueness in material model calibration using the virtual fields method. Comput Mater Sci 152:268–290. https://doi.org/10.1016/j.commatsci.2018.05.037
39. Jones EMC, Karlson KN, Reu PL (2019) Investigation of assumptions and approximations in the virtual fields method for a viscoplastic material model. Strain 55(4). https://doi.org/10.1111/str.12309
40. Lava P, Jones EMC, Wittevrongel L, Pierron F (2020) Validation of finite-element models using full-field experimental data: levelling finite-element analysis data through a digital image correlation engine. Strain 56(4). https://doi.org/10.1111/str.12350
41. Grédiac M, Sur F, Blaysat B (2016) The grid method for in-plane displacement and strain measurement: a review and analysis. Strain 52(3):205–243. https://doi.org/10.1111/str.12182
42. Pierron F, Grédiac M (2012) The virtual fields method. Springer
43. Balcaen R, Wittevrongel L, Reu PL, Lava P, Debruyne D (2017) Stereo-DIC calibration and speckle image generator based on FE formulations. Exp Mech 57(5):703–718. https://doi.org/10.1007/s11340-017-0259-1
44. Balcaen R, Reu PL, Lava P, Debruyne D (2017) Stereo-DIC uncertainty quantification based on simulated images. Exp Mech 57(6):939–951. https://doi.org/10.1007/s11340-017-0288-9
45. Rossi M, Pierron F (2012) On the use of simulated experiments in designing tests for material characterization from full-field measurements. Int J Solids Struct 49:420–435
46. Wang P, Pierron F, Rossi M, Lava P, Thomsen O (2016) Optimized experimental characterization of polymeric foam material using DIC and the Virtual Fields Method. Strain 52(1):59–79
47. Bouda P, Langrand B, Notta-Cuvier D, Markiewicz E, Pierron F (2019) A computational approach to design new tests for viscoplasticity characterization at high strain-rates. Comput Mech 64(6):1639–1654. https://doi.org/10.1007/s00466-019-01742-y
48. Lukić B, Saletti D, Forquin P (2020) Validation of the photomechanical spalling test in the case of non-linear dynamic response: application to a granite rock. Strain. https://doi.org/10.1111/str.12363
49. Xia K, Rosakis AJ, Kanamori H (2004) Laboratory earthquakes: the sub-Rayleigh-to-supershear rupture transition. Science 303(5665):1859–1861. https://doi.org/10.1126/science.1094022
50. Rosakis AJ, Xia K, Lykotrafitis G, Kanamori H (2007) Dynamic shear rupture in frictional interfaces: speeds, directionality, and modes. In: Treatise on Geophysics. Elsevier, pp 183–213. https://doi.org/10.1016/b978-0-444-53802-4.00072-5
51. Mello M, Bhat HS, Rosakis AJ, Kanamori H (2010) Identifying the unique ground motion signatures of supershear earthquakes: theory and experiments. Tectonophysics 493(3–4):297–326. https://doi.org/10.1016/j.tecto.2010.07.003
52. Gabuchian V, Rosakis AJ, Bhat HS, Madariaga R, Kanamori H (2017) Experimental evidence that thrust earthquake ruptures might open faults. Nature 545(7654):336–339. https://doi.org/10.1038/nature22045
53. Lu X, Lapusta N, Rosakis AJ (2009) Analysis of supershear transition regimes in rupture experiments: the effect of nucleation conditions and friction parameters. Geophys J Int 177(2):717–732. https://doi.org/10.1111/j.1365-246x.2009.04091.x
54. Geubelle P (1995) A spectral method for three-dimensional elastodynamic fracture problems. J Mech Phys Solids 43(11):1791–1824. https://doi.org/10.1016/0022-5096(95)00043-i
55. Liu Y, Lapusta N (2008) Transition of Mode II cracks from sub-Rayleigh to intersonic speeds in the presence of favorable heterogeneity. J Mech Phys Solids 56(1):25–50. https://doi.org/10.1016/j.jmps.2007.06.005
56. Singh RP, Parameswaran V (2003) An experimental investigation of dynamic crack propagation in a brittle material reinforced with a ductile layer. Opt Lasers Eng 40(4):289–306. https://doi.org/10.1016/s0143-8166(02)00089-1
57. Kanamori H, Rivera L (2006) Energy partitioning during an earthquake. In: Earthquakes: Radiated Energy and the Physics of Faulting. American Geophysical Union, pp 3–13. https://doi.org/10.1029/170gm03
58. Templeton EL, Rice JR (2008) Off-fault plasticity and earthquake rupture dynamics: 1. dry materials or neglect of fluid pressure changes. J Geophys Res 113(B9). https://doi.org/10.1029/2007jb005529
59. Dunham EM, Rice JR (2008) Earthquake slip between dissimilar poroelastic materials. J Geophys Res 113(B9). https://doi.org/10.1029/2007jb005405

60. Dieterich JH (2007) Applications of rate- and state-dependent friction to models of fault-slip and earthquake occurrence. In: Treatise on Geophysics. Elsevier, pp 93–110. https://doi.org/10.1016/b978-0-444-53802-4.00075-0
61. Reu PL (2010) Experimental and numerical methods for exact subpixel shifting. Exp Mech 51(4):443–452. https://doi.org/10.1007/s11340-010-9417-4
62. Wang Y, Lava P, Reu P, Debruyne D (2016) Theoretical analysis on the measurement errors of local 2d DIC: Part i temporal and spatial uncertainty quantification of displacement measurements. Strain 52(2):110–128
63. Wang Y, Lava P, Reu P, Debruyne D (2016) Theoretical analysis on the measurement errors of local 2d DIC: Part II assessment of strain errors of the local smoothing method-approaching an answer to the overlap question. Strain 52(2):129–147
64. Jones EMC, Iadicola MA (2018) A good practices guide for digital image correlation. Technical report. https://doi.org/10.32720/idics/gpg.ed1
65. Day SM, Dalguer LA, Lapusta N, Liu Y (2005) Comparison of finite difference and boundary integral solutions to three-dimensional spontaneous rupture. J Geophys Res 110(B12). https://doi.org/10.1029/2005jb003813
66. Samudrala O, Huang Y, Rosakis AJ (2002) Subsonic and intersonic shear rupture of weak planes with a velocity weakening cohesive zone. J Geophys Res Solid Earth 107(B8):7
67. Mello M, Bhat HS, Rosakis AJ (2016) Spatiotemporal properties of sub-Rayleigh and supershear rupture velocity fields: theory and experiments. J Mech Phys Solids 93:153–181. https://doi.org/10.1016/j.jmps.2016.02.031
68. Schreier HW, Sutton MA (2002) Systematic errors in digital image correlation due to undermatched subset shape functions. Exp Mech 42(3):303–310
69. Bornert M, Brémand F, Doumalin P, Dupré J-C, Fazzini M, Grédiac M, Hild F, Mistou S, Molimard J, Orteu J-J, Robert L, Surrel Y, Vacher P, Wattrisse B (2009) Assessment of digital image correlation measurement errors: methodology and results. Exp Mech 49(3):353–370. https://doi.org/10.1007/s11340-008-9204-7
70. Rubino V, Lapusta N, Rosakis A (2022) Intermittent lab earthquakes in dynamically weakening fault gouge. Nature 1–8
71. Mizoguchi K, Hirose T, Shimamoto T, Fukuyama E (2007) Reconstruction of seismic faulting by high-velocity friction experiments: an example of the 1995 Kobe earthquake. Geophys Res Lett 34(1)
72. Niemeijer A, Di Toro G, Nielsen S, Di Felice F (2011) Frictional melting of gabbro under extreme experimental conditions of normal stress, acceleration, and sliding velocity. J Geophys Res Solid Earth 116(B7)
73. Svetlizky I, Fineberg J (2014) Classical shear cracks drive the onset of dry frictional motion. Nature 509(7499):205–208
74. Xu S, Fukuyama E, Yamashita F (2019) Robust estimation of rupture properties at propagating front of laboratory earthquakes. J Geophys Res Solid Earth 124(1):766–787
75. Buades A, Coll B, Morel JM (2005) A review of image denoising algorithms, with a new one. Multiscale Model Simul 4(2):490–530. https://doi.org/10.1137/040616024
76. Buades A, Coll B, Morel J-M (2008) Nonlocal image and movie denoising. Int J Comput Vision 76:123–139. https://doi.org/10.1007/s11263-007-0052-1
77. Andrews DJ (1976) Rupture velocity of plane strain shear craks. J Geophys Res 81(32):5679–5687. https://doi.org/10.1029/JB081i032p05679
78. Palmer AC, Rice JR (1973) The growth of slip surfaces in the progressive failure of over-consolidated clay. Proc R Soc A: Math Phys Eng Sci 332(1591):527–548